

AquaROM: shape optimization pipeline for soft swimmers using parametric reduced order models

Journal Title
XX(X):1–22
©The Author(s) 2025
Reprints and permission:
sagepub.co.uk/journalsPermissions.nav
DOI: 10.1177/ToBeAssigned
www.sagepub.com/

SAGE

Mathieu Dubied^{1,2}, Paolo Tiso², Robert K. Katzschmann¹

Abstract

The efficient optimization of actuated soft structures, particularly under complex nonlinear forces, remains a critical challenge in advancing robotics. Simulations of nonlinear structures, such as soft-bodied robots modeled using the finite element method (FEM), often demand substantial computational resources, especially during optimization. To address this challenge, we propose a novel optimization algorithm based on a tensorial parametric reduced order model (PROM). Our algorithm leverages dimensionality reduction and solution approximation techniques to facilitate efficient solving of nonlinear constrained optimization problems. The well-structured tensorial approach enables the use of analytical gradients within a specifically chosen reduced order basis (ROB), significantly enhancing computational efficiency. To showcase the performance of our method, we apply it to optimizing soft robotic swimmer shapes. These actuated soft robots experience hydrodynamic forces, subjecting them to both internal and external nonlinear forces, which are incorporated into our optimization process using a data-free ROB for fast and accurate computations. This approach not only reduces computational complexity but also unlocks new opportunities to optimize complex nonlinear systems in soft robotics, paving the way for more efficient design and control.

Keywords

Modeling, Control, and Learning for Soft Robots, Soft Robot Materials and Design, Optimization and Optimal Control

1 Introduction

When designing mechanical systems, such as robots, MEMS, or wind turbines, engineers typically aim to find structures that exhibit optimal properties while respecting specific constraints. Instead of solely relying on testing physical prototypes of a given system, numerical simulations of these same prototypes are often less costly, faster, and easier to set up. In addition, simulations can provide useful information, such as gradients, to perform optimization of the system's properties in an automated fashion.

A typical way to simulate mechanical structures is to use the finite element method (FEM), which is based on the discretization of the original structure into finite elements (FEs). This approach, while expressive and accurate, often leads to high computational costs due to the large number of degrees of freedom (DoFs) of the resulting system. Moreover, these computational costs are notably increased when the system at hand is subject to nonlinear forces. In particular, large deformations of the structure lead to internal nonlinear forces, while contact with an external medium such as water or air gives rise to nonlinear drag forces. As a consequence, these large computational efforts might hinder the rapid prototyping and designing of new mechanical systems.

To reduce the computational costs of FEM simulations, model order reduction techniques are widely used. In such cases, the use of a reduced order model (ROM) allows for faster simulations as it uses significantly less DoFs compared to the initial full order model (FOM). If properly chosen, the selected DoFs used in the ROM are the most significant for the modeling of the studied structure, and, therefore,

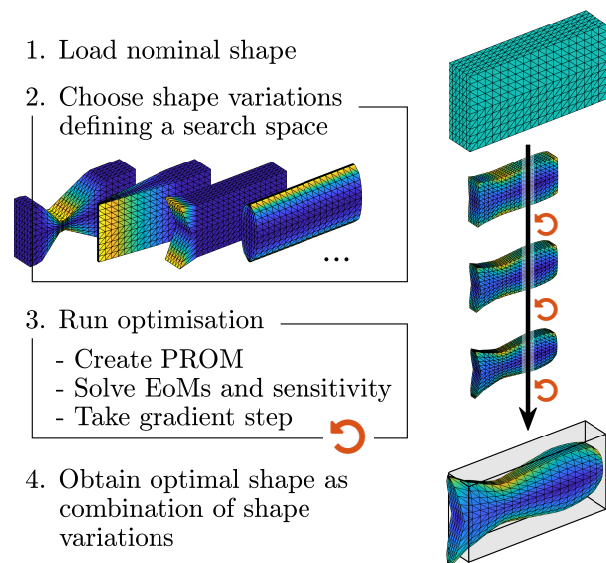


Figure 1. Optimization pipeline applied to the case of soft robotic fishes. Starting from a nominal shape, our pipeline solves a constrained optimization problem in a computationally efficient way by using a PROM. The pipeline results in an optimal shape that outperforms the nominal setting.

¹Soft Robotics Laboratory (SRL), ETH Zurich, Switzerland

²Chair in Nonlinear Dynamics, ETH Zurich, Switzerland

Corresponding author:

Robert K. Katzschmann, SRL, ETH Zurich, Switzerland

Email: rkk@ethz.ch

the simulations remain accurate while being faster. In this context, different approaches can be followed to select a reduced order basis (ROB) that can correctly capture the deformation of the original nonlinear system. In addition, it is even possible to include parameters describing important characteristics of the considered mechanical structure in the ROM, resulting in a parametric reduced order model (PROM). The key advantage of a PROM is that it only needs to be constructed once and remains valid for multiple, small variations in the system's parameters.

Building on this particularity, which enables gradient computation, we propose a methodology for embedding nonlinear internal and external forces into a PROM and to exploit its analytical gradients to perform design optimization. Building on our recent work using a tensorial approach to express internal nonlinear forces in PROMs (Marconi et al. 2021, 2020; Saccani et al. 2022), we expand this method to reduce other (external) nonlinear forces that are relevant for the systems we study in this paper. We leverage this approach to obtain well-structured analytical expressions of the various nonlinear forces acting on our system and embed their analytical gradients in a novel optimization pipeline. Because the nonlinear forces we consider show considerable diversity in their mathematical structure, we aim at providing a general pipeline that can easily be adapted to other case-specific nonlinear forces.

To showcase our method, we consider the task of finding optimal shapes of soft robotic fishes (Figure 1). This choice is motivated by three important characteristics of soft robots that make them suitable benchmarks for our modeling and optimization approaches: (1) soft robots are highly deformable, resulting in nonlinear internal elastic forces that can be accurately modeled using FEM-based approaches, (2) soft swimmers are subject to diverse nonlinear external forces which slow down simulations and create a need for ROMs to capture the dynamics more efficiently, and (3) finding optimal shapes is of practical relevance for roboticists and is known as a difficult design task. Our contribution can therefore be summarized as follows:

1. *Development and testing of a fast optimization pipeline:* Our optimization pipeline efficiently leverages the gradients of our PROM to find optimal design shapes. By showcasing, comparing, and discussing several numerical case studies, we show the benefits and limitations of our algorithm.
2. *Creation of a specific PROM for nonlinear hydrodynamic forces:* Our PROM contributes to related work by extending existing reduction methods to new external forces. In particular, the hydrodynamic forces expressed by Lighthill's elongated-body theory are considered (Lighthill 1971). Our work provides examples for the reduction of different nonlinear forces that can serve as a blueprint for other studies.

The remainder of this paper is structured as follows. After highlighting relevant related work in Section 2, we introduce the different nonlinear forces used in our framework in Section 3. These forces are first expressed at the finite element level and then reduced in Section 4 to obtain our PROM formulation. We then present our optimization pipeline in Section 5, and show our numerical

results in Section 6. We conclude this work by discussing the relevance of our numerical approach, its limitations, and important directions for future work in Section 7.

2 Related work

This section reviews the most relevant literature related to the methods and results presented in this paper. It is divided into three parts. First, we discuss previous work important for the simulation of soft robots, and in particular for the simulation of soft swimmers. Second, we present literature on FEM-based ROMs, which can be leveraged to reduce the computational burden associated with FEM simulations. As a third and final part, we discuss the task of optimizing the shape of soft swimmers, and highlight how this task relates to both FEM and ROM-based simulations.

2.1 Simulation of soft robotic fishes

In comparison to rigid robots, soft robots are difficult to model and simulate due to the infinite number of degrees of freedom of their state space and the large nonlinear deformations they undergo (Chen et al. 2023a; Laschi et al. 2012; Trivedi et al. 2008b). Methods to simulate soft robots can be divided into three main categories based on the type of models used to describe the robot dynamics. The first type of models consists of simplified models, such as the augmented rigid body model (Della Santina et al. 2020a,b), which is based on the piecewise constant curvature model (Webster III and Jones 2010). A second type of models relies on data collected on the robot itself (Huang et al. 2024; Bruder et al. 2025, 2019; Holsten et al. 2019; Reinhart and Steil 2016). Finally, a third type of models considers FEM as a way to simulate soft robots (Wang et al. 2024c; Qin et al. 2024; Du et al. 2021a; Duriez et al. 2016; Duriez 2013). This last type of models is considered in this work.

At their core, FEM approaches follow a few key steps: they discretize the structure at hand in small, finite elements (FEs), formulate equations for each FE considering the different forces applied to the structure, assemble the FE into a global system, and solve the resulting set of equations to describe quantities such as displacement over time. Following these steps, FEM approaches can effectively account for nonlinearities that arise from the large deformations of soft robots and the nonlinear behavior of the materials used to manufacture these robots (Tawk and Alici 2020; Pinskiel et al. 2024). In practice, however, achieving precise FEM-based simulations requires careful meshing and precise tuning of material parameters (Dubied et al. 2022). Even then, high-fidelity nonlinear FEM simulations are computationally expensive without model order reduction techniques (Navez et al. 2025; Goury et al. 2021). Therefore, simulations using FOMs are not directly suitable for control and fast prototyping tasks.

Before discussing model order reduction strategies in Section 2.2, we first focus on the specific modeling of soft robotic fishes, which are the mechanical structures that we study in this work. Due to their agile and efficient underwater movements, real fishes have inspired roboticists aiming to replicate these desirable characteristics in soft robotic designs (Katzschmann et al. 2016; Zhu et al. 2019; van den Berg et al. 2020; Wang et al. 2024b; Liu et al.

2025). Designing such robotic fishes is time-consuming and requires iterative fabrication and testing procedures. In this context, numerical simulations can fasten the process by enabling virtual design iterations and testing (Matthews et al. 2023; Spielberg et al. 2017). Nevertheless, using FEM-based simulations for soft robotic fishes presents significant challenges, particularly due to the complexities of fluid-structure interaction (FSI) in underwater environments (Nava et al. 2022). Due to this complexity, previous works modeling FSI using FEM typically restrict their attention to planar formulations (Curatolo and Teresi 2015; Gravert et al. 2022; Wang et al. 2024a) or use parametrized added-mass and drag forces (Liu et al. 2025).

When moving from 2-dimensional to 3-dimensional fish FEM simulations, the effects of hydrodynamics on the solid structure are often modeled using surrogate models (Min et al. 2019; Ma et al. 2021a). Practically, these models aim to approximate the thrust and drag caused by the fluid on the robot using heuristic rules. Alternatively, neural networks (Wandel et al. 2020; Zhang et al. 2022) and GPU-optimized solvers (Liu et al. 2022) have been used to simulate fluid-solid interactions. In this work, we consider Lighthill’s large-amplitude elongated-body theory (LAEBT) to model the interaction between the fluid and the fish movements (Lighthill 1971). The LAEBT models the thrust (or reactive) force produced by the locomotion of carangiform fish, considering the rate of change in momentum in the fluid domain surrounding the fish. The LAEBT, as well as its extensions, have been compared to computational fluid dynamics (CFD) simulations (Candelier et al. 2011, 2013) and real-world experiments (Wang et al. 2011; Li et al. 2014; Chen et al. 2023b). As a key contribution, we show in this work how to reduce the hydrodynamic forces stemming from the LAEBT into a PROM, enabling the faster solving of equations of motion.

2.2 ROMs for FEM-based simulations

Model order reduction (MOR) techniques have been developed to mitigate the computational costs associated with FEM simulations, especially when dealing with nonlinear and high-dimensional systems. In this context, reduced-order models (ROMs) provide an efficient way to approximate the behavior of complex mechanical systems while retaining sufficient accuracy for practical applications.

For systems with geometric and material nonlinearities, tensor-based formulations have recently emerged as powerful tools to represent internal forces in a polynomial and structured form. In particular, Marconi et al. (2020, 2021) introduced a nonlinear ROM framework based on a Neumann expansion of the deformation gradient, allowing internal elastic forces to be expressed as high-order tensors. This structure enables efficient evaluation and differentiation, which is essential for gradient-based optimization. The method has been further extended to include shape defects and parametric variations, thus broadening its applicability. Along with allowing analytical parametrization with respect to shape variations, the tensorial approach also avoids the bottleneck of the computation of the reduced nonlinear terms and therefore does not require hyper-reduction, as done for instance in Tiso et al. (2013).

Saccani et al. (2022) built upon this approach to perform sensitivity analysis of nonlinear frequency responses in structures with geometric imperfections. Their work demonstrated how the parametric ROM formulation can be used for fast and accurate computation of nonlinear dynamic responses under varying conditions. For multibody flexible systems, the mentioned approaches could be embedded into component mode synthesis methods (Karamooz Mahdiabadi et al. 2019; Wu et al. 2019; Wu and Tiso 2016).

ROMs have also proven valuable for soft robotics, where nonlinearities arise from both the material behavior and interactions with the environment. For example, Goury and Duriez (2018) proposed a data-driven MOR approach tailored to soft robots, enabling real-time control and simulation. Katzschmann et al. (2019a) applied ROMs in the context of soft robotic arms, using a reduced FEM model with a state observer for closed-loop control. More recently, Navez et al. (2025) proposed a MOR method for soft robots with contact-rich dynamics and a variety of actuators, further confirming the effectiveness of ROM-based approaches for simulation and control in such settings.

2.3 Shape optimization of soft swimmers

Equipped with reliable simulation frameworks, roboticists can design soft robots efficiently by first analyzing virtual designs, and in a second step proceed to the time-consuming manufacturing of these designs. Going one step further, differentiable simulators provide their users with gradients, allowing therefore the use of automated gradient-based optimization (Bächer et al. 2021).

Various differentiable frameworks suitable for the simulation of soft robots have recently emerged (Du et al. 2021b; Geilinger et al. 2020; Hu et al. 2019). Previous works allow for the co-design of structural and control parameters for situations with contact forces, but without using any ROM formulation (Du et al. 2021b; Geilinger et al. 2020; Hu et al. 2019; Hahn et al. 2019; Hu et al. 2020; Huang et al. 2021; Bern et al. 2019; Wang et al. 2024c). As an example, the DiffPD differentiable simulator (Du et al. 2021b) allows the automatic calibration of material parameters and control signals applied to soft structures modeled with FEM. The recent work by Navez et al. (2025) goes one step further by presenting a data-driven MOR method that can be used to optimize control and design parameters. The proposed method uses a neural network to learn a representation of soft robots based on a large dataset of FOM FEM simulations. In contrast, our pipeline does not require any prior FEM simulation or offline learning to construct the PROM, and we focus on a larger set of design parameters.

The work most similar to ours in terms of application is probably the DiffAqua pipeline developed by Ma et al. (2021a), which employs a differentiable framework to optimize the design of soft swimmers. It uses the Wasserstein barycenters to interpolate between different base shapes and find an optimal shape combination, using a FOM. On a methodological level, our optimization method is similar to the one proposed by Fröhlich et al. (2019), where a PROM is used to optimize shape parameters for linear systems. In comparison, we present a method that allows to include nonlinear forces in the PROM and the optimization pipeline. Importantly, our starting point is to express internal and

external forces using a full FE mesh and only then project them onto a reduced model for optimization, in contrast to approaches that formulate the optimization directly on low-order models such as Cosserat rod formulations (Trivedi et al. 2008a; Armanini et al. 2022).

Our work combines the different key elements mentioned above: shape optimization, data-free PROM, differentiable framework, and hydrodynamic forces acting as nonlinear forces. By combining these elements, we develop in this paper a fast and accurate optimization algorithm to find optimal soft swimmer shapes.

3 Polynomial forces at the finite element-level

In this section, we describe the forces we include in our FE model. After presenting the equations of motion (EoMs) of the FOM in Section 3.1, we derive polynomial expressions for the forces acting on the soft swimmers: the nonlinear internal forces (Section 3.2), the thrust force (Section 3.3), the drag force (Section 3.3) and the actuation force (Section 3.5). These forces, expressed at the element-level, are then reduced and included in the PROM in Section 4.

3.1 Nonlinear full order model

The nonlinear FE system we consider in this work is

$$M\ddot{\mathbf{u}} + C\dot{\mathbf{u}} + \mathbf{f}_{\text{int}}(\mathbf{u}) = \mathbf{f}_{\text{thrust}}(\mathbf{u}, \dot{\mathbf{u}}, \ddot{\mathbf{u}}) + \mathbf{f}_{\text{drag}}(\dot{\mathbf{u}}) + \mathbf{f}_{\text{act}}(\mathbf{u}, t), \quad (1)$$

where $\mathbf{u} \in \mathbb{R}^n$ is the nodal displacement vector, M the mass matrix, C the damping matrix, and \mathbf{f}_{int} the internal nonlinear forces. The external forces acting on the fish are separated into the thrust force $\mathbf{f}_{\text{thrust}}$, the drag force \mathbf{f}_{drag} and the actuation force \mathbf{f}_{act} . In the following, we denote vectors by bold lower case letters and matrices as well as tensors by bold upper case letters.

The FEM formulation used in this work includes a set of user-defined parameters that allows to describe shape variations of the original, *nominal* structure. These shape variations (see, e.g., Figure 1, and Figure 10) describe alternative FE meshes which we call *shape-varied* configurations. In our optimization framework (Section 5), the linear combinations of these shape-varied configurations defines our search space.

Following the approach presented by Marconi et al. (2021), the deformations of shape-varied meshes are described by two successive mappings, as shown in Figure 2. The first mapping, $\mathcal{F}_1(\mathbf{x}_0)$, describes the mesh deformation from the nominal configuration \mathbf{x}_0 to the shape-varied configuration \mathbf{u}_ξ , and the second mapping, $\mathcal{F}_2(\mathbf{x}_\xi, t)$, the deformation from the shape-varied configuration to the deformed configuration \mathbf{x} . This 2-steps approach is used to describe the different forces acting on the FE mesh, which we derive next.

3.2 Nonlinear internal forces

The nonlinear internal forces are formulated according to the approach presented by Marconi et al. (2021). Using the notation $D = \frac{\partial \mathbf{u}}{\partial \mathbf{x}_0}$ and $D_\xi = \frac{\partial \mathbf{u}_\xi}{\partial \mathbf{x}_0}$, together with the

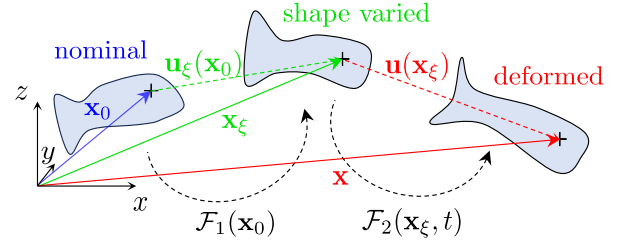


Figure 2. Nominal, shape-varied, and deformed configurations. The final deformed configuration can be expressed through two successive mappings: $\mathcal{F}_1(\mathbf{x}_0)$ and $\mathcal{F}_2(\mathbf{x}_\xi, t)$.

deformation gradients F_1 and F_2 corresponding to the mappings \mathcal{F}_1 and \mathcal{F}_2 respectively, the Green-Lagrange strain can be expressed as

$$E = \frac{1}{2}(F_2^\top F_2 - I) = \frac{1}{2}F_1^{-\top}(D + D^\top + D^\top D + D_\xi^\top D + D^\top D_\xi)F_1^{-1}.$$

The Green-Lagrange strain can be expressed as a polynomial by approximating the inverse deformation gradient F_1^{-1} using convergent Neumann series (Marconi et al. 2020, 2021). This polynomial form of the Green-Lagrange strain implies that the internal force \mathbf{f}_{int} is also polynomial in \mathbf{u} and \mathbf{u}_d . At the element-level of the FE assembly, the internal force is composed of three separate contributions:

$$\mathbf{f}_{\text{int}}^e = \mathbf{f}_1^e + \mathbf{f}_2^e + \mathbf{f}_3^e \in \mathbb{R}^{n_e},$$

where the superscript \star^e denotes element-level quantities and n_e is the number of DoFs in a single FE. These three contributions are given by

$$\mathbf{f}_1^e = {}_2\mathbf{K}(\mathbf{u}_\xi^e) \cdot \mathbf{u}^e,$$

$$\mathbf{f}_2^e = {}_3\mathbf{K}(\mathbf{u}_\xi^e) : (\mathbf{u}^e \otimes \mathbf{u}^e),$$

$$\mathbf{f}_3^e = {}_4\mathbf{K}(\mathbf{u}_\xi^e) \dot{ : } (\mathbf{u}^e \otimes \mathbf{u}^e \otimes \mathbf{u}^e),$$

where

$${}_2\mathbf{K}(\mathbf{u}_d^e) = {}_{2n}\mathbf{K} + {}_{3\xi}\mathbf{K} \cdot \mathbf{u}_\xi^e + {}_{4\xi\xi}\mathbf{K} : (\mathbf{u}_\xi^e \otimes \mathbf{u}_\xi^e), \quad (2a)$$

$${}_3\mathbf{K}(\mathbf{u}_d^e) = {}_{3n}\mathbf{K} + {}_{4\xi}\mathbf{K} \cdot \mathbf{u}_\xi^e + {}_{5\xi\xi}\mathbf{K} : (\mathbf{u}_\xi^e \otimes \mathbf{u}_\xi^e), \quad (2b)$$

$${}_4\mathbf{K}(\mathbf{u}_\xi^e) = {}_{4n}\mathbf{K} + {}_{5\xi}\mathbf{K} \cdot \mathbf{u}_\xi^e + {}_{6\xi\xi}\mathbf{K} : (\mathbf{u}_\xi^e \otimes \mathbf{u}_\xi^e). \quad (2c)$$

The subscripts of the tensors \mathbf{K} should be understood as follows:

- The number denotes the order of the tensor.
- The letter n denotes the fact that the tensor is computed for the nominal mesh.
- The letter ξ denotes the fact that the tensor multiplies the shape-varied vector \mathbf{u}_ξ , either once (ξ) or twice ($\xi\xi$).

The exact formulation of these tensors can be found in Marconi et al. (2021).

3.3 Thrust force

The interaction between the fluid and the fish is modeled using the Lighthill's elongated-body theory of fish

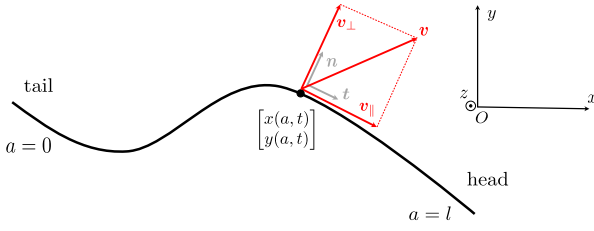


Figure 3. Reference frame used to derive the reactive force. The spine of the fish is observed from the top in this diagram.

locomotion (Lighthill 1971). While being a simplification of the complex solid-fluid interactions that can happen in reality, this model is derived using physics' first principles. In addition, this theory has been used to analyze the locomotion of fishes and underwater robots in practice (Wang et al. 2011; Li et al. 2014; Ma et al. 2021a; Eloy and Michelin 2024).

Figure 3 introduces the reference frame used to describe the hydrodynamic forces acting on the fish. Particularly important is the use of the Lagrangian coordinate a which has a value of 0 at the tail of the fish, and l at its head.

The Lighthill's elongated-body theory of fish locomotion derives a force called the *reactive force*, which captures the effects of inertial forces on the fish locomotion in inviscid flows. This reactive force, responsible for the thrust, is given by

$$\begin{aligned} \begin{bmatrix} f_x \\ f_y \end{bmatrix} &= \left[-\tilde{m}v_{\perp}v_{\perp}\mathbf{n} + \frac{1}{2}\tilde{m}v_{\perp}^2\mathbf{t} \right]_{a=0} \\ &\quad - \frac{d}{dt} \int_0^l \tilde{m}v_{\perp}\mathbf{n} da, \\ &= \mathbf{f}_{\text{tail}} + \mathbf{f}_{\text{spine}} \end{aligned} \quad (3)$$

where \mathbf{t} is the unit vector tangential to the spine pointing in the direction of the head, and \mathbf{n} is the unit vector normal to the spine (see Figure 3 for the other symbols). In addition, \tilde{m} is the virtual mass of the considered cross-section of the fish. According to Lighthill (1971), this virtual mass is captured by the expression

$$\tilde{m} = \frac{\pi}{4}\rho d^2, \quad (4)$$

where ρ is the density of the fluid and d the cross-section's depth in the z -direction.

In the following, we denote the first part of the reactive force (3) as the *tail force* (at $a = 0$) and the second part as the *spine force*, which we combine to obtain the *thrust force* $\mathbf{f}_{\text{thrust}}$ in the EoMs (1). Moreover, we assume that at the tail ($a = 0$), the perpendicular velocity v_{\perp} is much larger than the tangential velocity v_{\parallel} (Wang et al. 2011). Next, we formulate the tail and spine force at the element-level of the FE model, after defining which nodes of the FE mesh are subject to these forces. When not necessary, we omit the superscript \star^e to present more readable expressions.

3.3.1 Selection of nodes As Lighthill (1971) derives the reactive force by focusing on the spine of the fish, we select *spine nodes* in the FE mesh, to which the reactive force (3) is applied. We rely on a symmetric meshing of the nominal structure, which therefore contains clearly defined spine nodes located on the symmetry axis. For each successive pair of spine nodes, we attribute a single FE which we include in

a set of *spine elements*. These spine elements are then used to apply the tail and spine forces, as described below.

3.3.2 Tail force The tail force is applied at the tail node, which is part of the spine element located at the extremity of the fish ($a = 0$). At this element, and with the assumption that $v_{\perp} \gg v_{\parallel}$ (Wang et al. 2011), the tail force is

$$\begin{aligned} \mathbf{f}_{\text{tail}}^e &= \frac{1}{2}\tilde{m}v_{\perp}^2\mathbf{t}^e = \frac{1}{2}\tilde{m}[(\mathbf{v} \cdot \mathbf{n}^e)^2\mathbf{t}^e] \\ &= \frac{1}{2}\tilde{m}w^3[(\mathbf{A}\dot{\mathbf{u}})^{\top}\mathbf{R}\mathbf{B}\mathbf{x}]^2\mathbf{B}\mathbf{x}, \end{aligned} \quad (5)$$

with $\mathbf{x} = \mathbf{x}_0 + \mathbf{u}_{\xi} + \mathbf{u}$ (see Figure 2) and where $\mathbf{t}^e, \mathbf{n}^e \in \mathbb{R}^{n^e}$ are the element versions of the 3D tangential vectors \mathbf{t} and \mathbf{n} . In addition, the matrix \mathbf{A} selects the component of $\dot{\mathbf{u}}$ corresponding to the tail DoFs, \mathbf{B} is used to create the tangential vector \mathbf{t}^e , and \mathbf{R} is a rotation matrix. The factor w stems from the normalization of the vectors \mathbf{t}^e and \mathbf{n}^e , assuming that the length of the spine is constant.

3.3.3 Spine force The spine force is applied to each spine element. For a given spine FE, the force at the element-level is described as

$$\begin{aligned} \mathbf{f}_{\text{spine}}^e &= -\frac{d}{dt} \int_0^l \tilde{m}(\mathbf{A}\dot{\mathbf{u}})^{\top}\mathbf{R}\mathbf{B}\mathbf{x}w\mathbf{R}\mathbf{B}\mathbf{x}w da \\ &= -\tilde{m}w \frac{d}{dt} [(\mathbf{A}\dot{\mathbf{u}})^{\top}\mathbf{R}\mathbf{B}\mathbf{x}\mathbf{R}\mathbf{B}\mathbf{x}] \\ &= -\tilde{m}w \left[(\mathbf{A}\ddot{\mathbf{u}})^{\top}\mathbf{R}\mathbf{B}\mathbf{x}\mathbf{R}\mathbf{B}\mathbf{x} \right. \\ &\quad \left. + (\mathbf{A}\dot{\mathbf{u}})^{\top}\mathbf{R}\mathbf{B}\dot{\mathbf{u}}\mathbf{R}\mathbf{B}\mathbf{x} \right. \\ &\quad \left. + (\mathbf{A}\dot{\mathbf{u}})^{\top}\mathbf{R}\mathbf{B}\mathbf{x}\mathbf{R}\mathbf{B}\dot{\mathbf{u}} \right]. \end{aligned} \quad (6)$$

3.3.4 Virtual mass The virtual mass \tilde{m} (4) of a given cross-section of the fish depends on the considered cross-section depth d . For each spine element, we match a single dorsal node with z -coordinate $z_0^{\text{max}} + z_{\xi}^{\text{max}}$. This allows us to compute the virtual mass attributed to a given spine element as

$$\tilde{m} = \frac{\pi}{4}\rho d^2 = \frac{\pi}{4}\rho(2z_0^{\text{max}} + 2z_{\xi}^{\text{max}})^2.$$

3.4 Drag force

While the reactive force (3) derived by Lighthill (1971) accounts for the inertial interaction between the fluid and the fish, it considers inviscid conditions where no drag occurs. We therefore enhance our model with a form drag based on the shape of the fish. Specifically, we apply a force at each element located on the skin of the fish similarly to the approach of Ma et al. (2021a) and Min et al. (2019). The drag force depends on the orientation of the surface elements and the overall fish velocity in the forward swimming direction (x -direction):

$$\mathbf{f}_{\text{drag}} = -\frac{1}{2}\rho AC_d(\alpha)\|\mathbf{v}_x\|^2\mathbf{d}_{\text{swim}},$$

where A is the area of the skin surface, C_d is a drag coefficient depending on the angle of attack α of the considered surface, and \mathbf{d}_{swim} is a unit vector pointing in the forward swimming direction. The velocity \mathbf{v}_x is measured at the fish head. The drag coefficient is symmetric with respect to α and expressed by analyzing the shape-varied

configuration at rest as

$$\begin{aligned} C_d(\alpha) &= \cos(2\alpha - \pi) + 1 \\ &= \cos(2\arccos(\mathbf{n} \cdot \mathbf{d}_{\text{swim}}) - \pi + \pi) + 1 \\ &= 2(\mathbf{n} \cdot \mathbf{d}_{\text{swim}})^2. \end{aligned}$$

In contrast to the tail force (5) and the spine force (6), the drag force is not a polynomial in \mathbf{u}_ξ . As a polynomial force is required to build our PROM (see Section 4), we approximate the drag force using a Taylor approximation up to the third order around the nominal structure $\mathbf{u}_\xi = \mathbf{0}$. The Taylor series coefficients are in this case tensors \mathbf{T} whose analytical form can be found using a computer algebra system (CAS) offline (Mathematical in our case). This results in the following drag force at the element-level:

$$\mathbf{f}_{\text{drag}}^e = \left({}_3\mathbf{T} + {}_4\mathbf{T} \cdot \mathbf{u}_\xi + {}_5\mathbf{T} : (\mathbf{u}_\xi \otimes \mathbf{u}_\xi) \right) : (\dot{\mathbf{u}} \otimes \dot{\mathbf{u}}). \quad (7)$$

3.5 Actuation force

The actuation force \mathbf{f}_{act} is inspired by the muscle model used by Du et al. (2021b) and Min et al. (2019). This approach allocates an additional spring-like energy to specific elements of the mesh, called *muscle elements*, which together form muscles that can contract or extend. We allocate the following energy to the muscle elements:

$$E = \frac{k}{2} a V^e \|\mathbf{F} \cdot \mathbf{m}\|^2, \quad (8)$$

where k can be understood as a spring stiffness, a is an actuation signal, V^e is the volume of the element, \mathbf{F} is the deformation gradient, and \mathbf{m} is the direction of actuation defined for the undeformed mesh element. Extension occurs for $a < 0$, and contraction occurs for $a > 0$. For simplicity, we consider V^e as a constant for each element and compute it based on the nominal configuration of the fish. Limitations of this approach are further discussed in Section 6.3.

Before deriving an expression for the actuation forces \mathbf{f}_{act} from the energy (8), we express this energy in a convenient tensorial form. Using a first order Neumann expansion as in Marconi et al. (2021), we can approximate the deformation gradient as

$$\mathbf{F} = \mathbf{F}_2 \mathbf{F}_1 \approx \mathbf{I} + \mathbf{D}_\xi + \mathbf{D} - \mathbf{D} \mathbf{D}_\xi^2.$$

Neglecting the $\mathcal{O}(\mathbf{D}_d^2)$ terms, we get

$$\mathbf{F} \approx \mathbf{I} + \mathbf{D}_\xi + \mathbf{D}. \quad (9)$$

The muscle energy (8) can be written using the obtained deformation gradient (9):

$$\begin{aligned} E &= \frac{k}{2} a V^e \mathbf{m}^\top \mathbf{F}^\top \mathbf{F} \mathbf{m} \\ &= \frac{k}{2} a V^e \mathbf{m}^\top (\mathbf{I} + \mathbf{D} + \mathbf{D}^\top + \mathbf{D}^\top \mathbf{D} \\ &\quad + \mathbf{D}_\xi + \mathbf{D}_\xi^\top + \mathbf{D}_\xi^\top \mathbf{D}_\xi + \mathbf{D}_\xi^\top \mathbf{D} + \mathbf{D}^\top \mathbf{D}_\xi) \mathbf{m}. \end{aligned} \quad (10)$$

We note that the matrix described by the expression in the parentheses is symmetric. At the element-level, we can resort to the shape function derivatives matrix $\mathbf{G} \in \mathbb{R}^{9 \times n_e}$ to express the terms in (9). This can be done using the Voigt

notation, which we denote with a subscript \star_V . We first express the matrices of (10) using in the Voigt notation:

$$\begin{aligned} \mathbf{I} &\longleftrightarrow \mathbf{I}_V \\ \mathbf{D} + \mathbf{D}^\top + \mathbf{D}^\top \mathbf{D} &\longleftrightarrow (2\mathbf{H} + \mathbf{A}_1(\boldsymbol{\theta}))\boldsymbol{\theta} \\ \mathbf{D}_\xi + \mathbf{D}_\xi^\top + \mathbf{D}_\xi^\top \mathbf{D}_\xi &\longleftrightarrow (2\mathbf{H} + \mathbf{A}_1(\boldsymbol{\theta}_\xi))\boldsymbol{\theta}_\xi \\ \mathbf{D}_\xi^\top \mathbf{D} + \mathbf{D}^\top \mathbf{D}_\xi &\longleftrightarrow 2\mathbf{A}_1(\boldsymbol{\theta}_\xi)\boldsymbol{\theta}, \end{aligned}$$

where $\boldsymbol{\theta}$ and $\boldsymbol{\theta}_d$ are the vectorized forms of \mathbf{D} and \mathbf{D}_d , e.g., $\boldsymbol{\theta} = [u_{,x} \ u_{,y} \ u_{,z} \ v_{,x} \ v_{,y} \ v_{,z} \ w_{,x} \ w_{,y} \ w_{,z}]^\top$. The matrices $\mathbf{I}_V, \mathbf{H}, \mathbf{A}_1(\boldsymbol{\theta}), \mathbf{A}_1(\boldsymbol{\theta}_\xi)$ are given in Section A.

The Voigt notation allows us to express the muscle energy as

$$E_V = \frac{k}{2} a V^e \mathbf{m}_V^\top [\mathbf{I}_V + (2\mathbf{H} + \mathbf{A}_1(\boldsymbol{\theta}))\boldsymbol{\theta} + (2\mathbf{H} + \mathbf{A}_1(\boldsymbol{\theta}_\xi))\boldsymbol{\theta}_\xi + 2\mathbf{A}_1(\boldsymbol{\theta}_\xi)\boldsymbol{\theta}], \quad (11)$$

with $\mathbf{m}_V = [m_x^2, m_y^2, m_z^2, m_x m_y, m_x m_z, m_y m_z]^\top$. We can use the shape function derivatives \mathbf{G} to express (11) as an explicit function of the displacement \mathbf{u} at the element-level:

$$\begin{aligned} E_V &= \frac{k}{2} a V^e \mathbf{m}_V^\top [\mathbf{I}_V + (2\mathbf{H} + \mathbf{L}_1 \cdot \boldsymbol{\theta})\boldsymbol{\theta} \\ &\quad + (2\mathbf{H} + \mathbf{L}_1 \cdot \boldsymbol{\theta}_\xi)\boldsymbol{\theta}_\xi + 2\mathbf{L}_1 \cdot \boldsymbol{\theta}_\xi \boldsymbol{\theta}] \\ &= \frac{k}{2} a \mathbf{m}_V^\top [\mathbf{I}_V + (2\mathbf{H} + \mathbf{L}_1 \cdot \mathbf{G} \mathbf{u})\mathbf{G} \mathbf{u} \\ &\quad + (2\mathbf{H} + \mathbf{L}_1 \cdot \mathbf{G} \mathbf{u}_\xi)\mathbf{G} \mathbf{u}_\xi + 2\mathbf{L}_1 \cdot \mathbf{G} \mathbf{u}_\xi \mathbf{G} \mathbf{u}], \end{aligned}$$

where \mathbf{L}_1 is a sparse third order tensor. Its exact composition is given in Section A. The operation between the tensor \mathbf{L}_1 and the vectors $\mathbf{G} \mathbf{u}$ and $\mathbf{G} \mathbf{u}_\xi$ is a contraction, which is best expressed using Einstein's notation:

$$\begin{aligned} E_V &= \frac{k}{2} a V^e m_{V,i} [I_{V,i} + (2H_{ij} + L_{1,ijk} G_{kl} u_l) G_{jm} u_m \\ &\quad + (2H_{ij} + L_{1,ijk} G_{kl} u_{\xi,l}) G_{jm} u_{\xi,m} \\ &\quad + 2L_{1,ijk} G_{kl} u_{\xi,l} G_{jm} u_m]. \end{aligned}$$

Finally, we can take the derivative of the muscle energy to get the corresponding actuation forces at the element-level, as follows:

$$\begin{aligned} f_{\text{act},L}^e &= \frac{dE_V}{du_L} \\ &= \frac{k}{2} a V^e m_{V,i} \left[(2H_{ij} + L_{1,ijk} G_{kl} u_l) G_{jL} \right. \\ &\quad \left. + L_{1,ijk} G_{kL} G_{jm} u_m + 2L_{1,ijk} G_{kl} u_{d,l} G_{jL} \right], \end{aligned} \quad (12)$$

where $f_{\text{act},L}^e$ is the component L of the actuation force \mathbf{f}_{act} at the element-level.

4 Reduction of nonlinear forces in PROM

In this section, we present our PROM, which allows to obtain a reduced order version of the EoMs (1), i.e.,

$$\begin{aligned} \mathbf{M}^r \ddot{\boldsymbol{\eta}} + \mathbf{C}^r \dot{\boldsymbol{\eta}} + \mathbf{f}_{\text{int}}^r(\boldsymbol{\eta}) &= \mathbf{f}_{\text{thrust}}^r(\boldsymbol{\eta}, \dot{\boldsymbol{\eta}}, \ddot{\boldsymbol{\eta}}) \\ &\quad + \mathbf{f}_{\text{drag}}^r(\dot{\boldsymbol{\eta}}) + \mathbf{f}_{\text{act}}^r(\boldsymbol{\eta}, t), \end{aligned} \quad (13)$$

where $\boldsymbol{\eta} \in \mathbb{R}^m$ entails the DoFs of the reduced system with dimension $m \ll n$, and the superscript r denotes

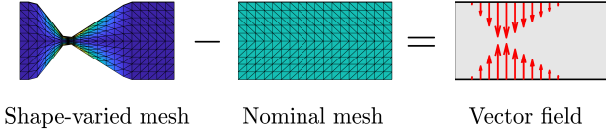


Figure 4. Procedure for populating the matrix U used to describe the shape-varied configuration $\mathbf{u}_\xi = U\xi$. After defining a shape-varied mesh, we subtract the nominal node positions to obtain a vector field. This vector field is stored as a column of U . By defining multiple vector field in the different columns of U , we can scale and combine them by multiplying U with the parameter vector ξ to obtain the different shape-varied configurations \mathbf{u}_ξ .

reduced quantities. To obtain these reduced quantities, the contribution of each element-level force is projected onto a ROB through a Galerkin projection. After presenting how we build our ROB (Section 4.1), we derive the reduced version of the forces introduced in Section 3 at the element-level (Section 4.2, 4.3, 4.4, and 4.5). The reduced element-level objects (e.g., tensors) can then simply be summed to obtain the EoMs (13) associated with the PROM.

4.1 Reduced order basis

The m basis vectors of the reduced order basis (ROB), which we describe in this section, are grouped in the matrix $V \in \mathbb{R}^{n \times m}$. The ROB described by V can be used to approximate the FOM displacement \mathbf{u} using the reduced order displacement η as $\mathbf{u} \approx V\eta$. Similarly, a basis can be created for the user-defined m_ξ shape variations as $\mathbf{u}_\xi = U\xi$ with $U \in \mathbb{R}^{n \times m_\xi}$. We refer to the vector ξ as *parameter vector*. Figure 4 shows how the matrix U is constructed by concatenating multiple basis vectors describing different shape variations. These shape variations are linearly combined to obtain the shape-varied configuration, through the operation $\mathbf{u}_\xi = U\xi$.

Following the work of Marconi et al. (2020, 2021); Saccani et al. (2022), we use a combination of vibration modes (VMs), modal derivatives (MDs), as well as shape variation parameter sensitivities (PSs) as basis vectors to construct our ROB. The VMs, MDs and PSs are stored in the matrices Φ , Θ and Ξ , respectively, and are assembled in $V = [\Phi, \Theta, \Xi]$ to obtain the ROB. To improve the numerical properties of the ROB, we orthonormalize V .

The VMs are obtained by considering the following linearized undamped system:

$$M\ddot{\mathbf{u}} + \mathbf{K}\mathbf{u} = \mathbf{0}, \quad (14)$$

where \mathbf{K} is the tangent stiffness matrix. The solutions to the differential equation (14) can be found by solving the related eigenvalue problem

$$(\mathbf{K} - \omega_i^2 \mathbf{M})\phi_i = \mathbf{0}. \quad (15)$$

where ω_i is the i -th eigenvalue, and ϕ_i is the i -th eigenvector, which corresponds to the i -th column of Φ .

The MDs incorporated in the ROB are computed from the derivative of (15) with respect to the displacement \mathbf{u} :

$$(\mathbf{K} - \omega_i^2 \mathbf{M}) \frac{\partial \phi_i}{\partial u_j} + \left(\frac{\partial \mathbf{K}}{\partial u_j} - \frac{\partial \omega_i}{\partial u_j} \right) \phi_i = \mathbf{0}.$$

The enhancement of the ROB with the MDs $\theta_{ij} = \frac{\partial \phi_i}{\partial u_j}$ allows to capture part of the effects of the nonlinear system. The quantities θ_{ij} are the element of the matrix Θ .

Finally, the PSs are obtained in a similar way as the MDs, but this time considering the differentiation of (15) with respect to the shape variation parameter vector ξ :

$$(\mathbf{K} - \omega_i^2 \mathbf{M}) \frac{\partial \phi_i}{\partial \xi_j} + \left(\frac{\partial \mathbf{K}}{\partial \xi_j} - \frac{\partial \omega_i}{\partial \xi_j} \right) \phi_i = \mathbf{0}.$$

Solving for $\frac{\partial \phi_i}{\partial \xi_j}$ allows to include the PSs in our ROB as elements of the matrix Ξ . Both the MDs and PSs are obtained in their static form computed on the nominal structure (see Jain et al. 2017, Section 3.3 for details).

A notable advantage of this choice of ROB is the fact that its construction is data-free, meaning that we do not rely on any simulation of the FOM or observation of a real structure to obtain the PROM, which can be numerically and time-costly operations.

4.2 Reduced internal forces

The reduced version of the internal force at the element-level consists of the projection of the tensors \mathbf{K} (2) onto the ROB. These reduced tensors are directly taken from previous work (Marconi et al. 2021).

4.3 Reduced thrust force

The reduced version of the thrust force, consisting of the tail force (5) and the spine force (6), is obtained through a projection onto the ROB, as shown below.

4.3.1 Tail force The reduced version of the element-level tail force (5) is

$$\mathbf{f}_{\text{tail}}^r = \frac{1}{2} \tilde{m} w^3 [(\mathbf{A}\mathbf{V}\eta)^\top \mathbf{R}\mathbf{B}(\mathbf{x}_0 + U\xi + \mathbf{V}\eta)]^2 \mathbf{V}^\top \mathbf{B}(\mathbf{x}_0 + U\xi + \mathbf{V}\eta).$$

The virtual mass is computed as

$$\tilde{m} = \frac{\pi}{4} \rho d^2 = \frac{\pi}{4} \rho (2z_0^{\max} + 2U^{\max} \xi)^2,$$

where U^{\max} is the row of U corresponding to the DOF of z_0^{\max} .

4.3.2 Spine force The reduced version of the spine force (6) is best described using Einstein's notation. The I -th component of the element-level force is given by

$$\begin{aligned} f_I^r = & -\frac{\pi}{4} \rho (2z_0^{\max} + 2U_k^{\max} \xi_k)^2 w \\ & \cdot V_{iI} \{ (A_{mn} V_{nj} \ddot{\eta}_j) R_{mp} B_{pq} \mathbf{x}_q^r R_{is} B_{st} \mathbf{x}_t^r \\ & + (A_{mn} V_{nj} \dot{\eta}_j) R_{mp} B_{pq} V_{qr} \dot{\eta}_r R_{is} B_{st} \mathbf{x}_t^r \\ & + (A_{mn} V_{nj} \dot{\eta}_j) R_{mp} B_{pq} \mathbf{x}_q^r R_{is} B_{st} V_{tu} \dot{\eta}_u \}, \end{aligned} \quad (16)$$

where

$$\mathbf{x}_q^r = x_{0,q} + U_{qr} \xi_r + V_{qr} \eta_r.$$

To be able to sum the contribution of each spine element when building the PROM, it is necessary to express each coefficient of (16) as separate tensors. These tensors are given in Section B.

4.4 Reduced drag force

The reduced version of the drag force (7) is given by

$$\mathbf{f}_{\text{drag}}^r = ({}_3\mathbf{T}^r + {}_4\mathbf{T}^r \cdot \boldsymbol{\xi} + {}_5\mathbf{T}^r : (\boldsymbol{\xi} \otimes \boldsymbol{\xi})) : (\dot{\boldsymbol{\eta}} \otimes \dot{\boldsymbol{\eta}}),$$

with, using Einstein notation,

$$\begin{aligned} {}_3T_{IJK}^r &= V_{iI}^e {}_3T_{ijk} V_{jJ}^e V_{kK}^e, \\ {}_4T_{IJKL}^r &= V_{iI}^e {}_4T_{ijkl} U_{jJ} V_{kK} V_{lL}^e, \\ {}_5T_{IJKLM}^r &= V_{iI}^e {}_5T_{ijklm} U_{jJ} U_{kK} V_{lL} V_{mM}^e, \end{aligned}$$

and where we explicitly use V^e to show that we use the part of \mathbf{V} corresponding to the concerned element.

4.5 Reduced actuation force

Finally, the reduced counter-part of the element-level actuation force (12) is, using Einstein notation,

$$\mathbf{f}_L^r = \frac{k}{2} a V^e ({}_1B_L + {}_2n B_{Li} \eta_i + {}_2\xi B_{Li} \xi_i)$$

where

$$\begin{aligned} {}_1B_I^e &= 2V_{nI}^e m_{V,i} H_{ij} G_{jn} \\ {}_2n B_{IJ}^e &= V_{nI}^e m_{V,i} (L_{1,ijk} G_{kl} V_{lJ}^e G_{jn} \\ &\quad + L_{1,ijk} G_{kn} G_{jm} V_{mJ}^e) \\ {}_2\xi B_{IJ}^e &= V_{nI}^e m_{V,i} (L_{1,ijk} G_{kn} G_{jm} U_{mJ}^e \\ &\quad + 2L_{1,ijk} G_{kl} U_{lJ}^e G_{jn}). \end{aligned}$$

5 Optimization using PROM gradients

In this section, we present our optimization pipeline (Figure 5), which leverages the PROM developed in Section 4. The pipeline starts with the upload of a nominal mesh and the definition of shape variations. The linear combination of these shape variations is defined by the parameter vector $\boldsymbol{\xi}$ (see Figure 4 and Section 4.1). Then, a first PROM is built based on this nominal mesh.

Based on the search parameters included in the vector $\boldsymbol{\xi}$, the optimization objective is the maximization of the distance swam by the fish during a fixed time horizon. Specifically, the cost function to minimize is

$$L = \sum_{i=n}^N -\mathbf{d}_{\text{swim}} \cdot \mathbf{V} \boldsymbol{\eta}_i(\boldsymbol{\xi}), \quad (17)$$

where \mathbf{d}_{swim} is the swimming direction expressed at the assembly-level, and the indices $i = n, n+1, \dots, N$ correspond to discrete time steps for which the solutions of the EoMs are computed. Our PROM formulation allows to use gradient descent to find local minima of the cost function. In particular, the gradient of the cost function is given by

$$\nabla L = \sum_{i=n}^N -\mathbf{d}_{\text{swim}} \cdot \mathbf{V} \mathbf{S}_i, \quad (18)$$

where

$$\mathbf{S} = \frac{d\boldsymbol{\eta}}{d\boldsymbol{\xi}} \quad (19)$$

is referred to as the *sensitivity* and describes how the solution $\boldsymbol{\eta}$, computed for the nominal shape, changes for

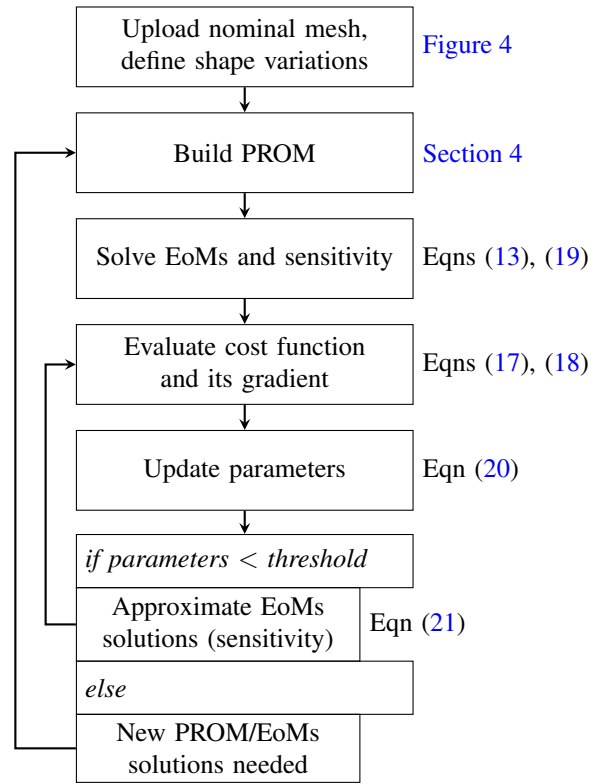


Figure 5. Optimization pipeline described in Section 5. The algorithm runs until convergence.

infinitesimal changes in the parameters $\boldsymbol{\xi}$. It can be obtained by solving as a separate ordinary differential equation (ODE) or more efficiently directly when solving the EoMs as shown by Bruls and Eberhard (2008). This step relies on the analytical expressions of the force derivatives, which can easily be obtained due to the tensorial structure of the reduced forces. In addition, we include barrier functions in the cost function (17) to be able to add linear constraints to the parameter vector $\boldsymbol{\xi}$.

The gradient of the cost function is then used to update the parameter vector $\boldsymbol{\xi}$. Denoting this vector at a given optimization step k as $\boldsymbol{\xi}_k$, the algorithm performs a gradient descent step with user-defined learning rate γ ,

$$\boldsymbol{\xi}_{k+1} = \boldsymbol{\xi}_k - \gamma \mathbf{W}_k \nabla L_k, \quad (20)$$

where \mathbf{W}_k is a diagonal weight matrix which is adapted during optimization to ensure convergence and constraint satisfaction. More precisely, it decreases the learning rate along specific directions if constraints are active in these directions. The computed sensitivity is also used to approximate the EoMs solutions in a neighborhood of the nominal solution $\boldsymbol{\eta}_0$ for the updated parameter vector $\boldsymbol{\xi}_{k+1}$:

$$\boldsymbol{\eta}_{k+1} \approx \boldsymbol{\eta}_0 + \mathbf{S} \cdot \boldsymbol{\xi}_{k+1}. \quad (21)$$

Because the approximation (21) is only valid in the vicinity of the nominal solution $\boldsymbol{\eta}_0$, the pipeline checks if the updated parameters in $\boldsymbol{\xi}_{k+1}$ are above a certain threshold. If this is the case, it builds a new PROM, considering the updated fish shape described by $\boldsymbol{\xi}_{k+1}$ as the new nominal shape. This algorithm runs until it reaches convergence, i.e., until the cost function does not change between successive optimization steps.

6 Results and discussion

To demonstrate the benefits of our approach, we present three types of numerical experiments. Firstly, Section 6.1 describes the chosen ROB and shows how the FOM, ROM and PROM relate in terms of computational costs and accuracy. Secondly, Section 6.2 applies the optimization pipeline developed in Section 5 to find optimal fish shapes for different numbers of search parameters. Finally, Section 6.3 extends the shape optimization pipeline to account for actuation signal optimization, enabling to tackle multi-objective optimization. Our simulations are performed using the open-source FEM package “YetAnotherFEcode” for Matlab (Jain et al. 2022), which we extended with the material presented above. The numerical case studies are run on a laptop equipped with an AMD Ryzen 7 PRO 6850U CPU with 32 GB of RAM, and the code is available online (<https://github.com/srl-ethz/AquaROM>).

6.1 Simulation setup and model comparisons

In this section, we report the simulation setup used for our case studies and assess its accuracy. The key elements of the simulation setup are: the nominal FEM structure and its properties (Section 6.1.1), the ROB selection (Section 6.1.2), and the solver parameters (Section 6.1.3). The simulation framework enables the fast solving of high-accuracy (P)ROMs (Section 6.1.4).

6.1.1 FEM nominal structure Each of our numerical experiments starts with the nominal structure depicted in Figure 6. It consists of a rectangular block equipped with two muscles. The elements of these muscles contract and extend according to the actuation forces described in Section 3.5. The head is rigid, following existing robotic designs (e.g. Katzschmann et al. 2018; Gravert et al. 2024).

The simulations are performed using a Saint Venant-Kirchhoff constitutive model and linear tetrahedra FEs, the numbers of which vary across the numerical experiments. The Saint Venant-Kirchhoff model is computationally easy to compute but can lead to poor behavior for large strains. In the nominal case, the maximum principal strain is less than 5% and localized in a few FEs in the outer layer of the structure, which justifies its use in our case studies. In particular, the tail’s tip reach large deformations (in the order of 50% of the body’s width), but the maximum strain remains small. We discuss extensions to other constitutive models (e.g., co-rotated or Neo-Hookean) and larger strains as future work in Section 7.

In the simulation and optimization case studies, we focus on forward swimming behaviors: the first part of the fish, composed of the rigid head, is constrained in the vertical and lateral directions so that it can only move in the forward or backward direction. The imposed motion constraints reflect the typical locomotion patterns observed in real fishes during steady forward swimming (Shelton et al. 2014). Focusing on forward swimming allows us to provide an intuitive illustration of the PROM-based optimization pipeline developed in Section 5. While the underlying force reduction and optimization framework readily extend to more complex swimming tasks, analyzing such scenarios lies outside the scope of this paper, as they typically require more

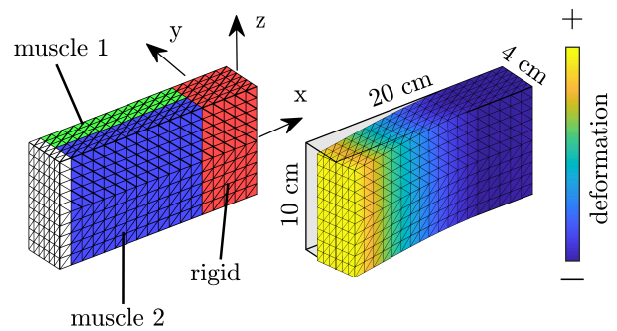


Figure 6. Nominal structure with a length of 20cm, a width of 4cm, and a height of 10cm. The left image shows the two muscles (green and blue), as well as the rigid part of the structure (red). The right image shows the first vibration mode (VM), which is an oscillation of the fish’ tail.

advanced control strategies (e.g., Min et al. 2019; Liu et al. 2022).

6.1.2 ROB selection The ROB used for our PROM consists of a rigid body mode along the forward direction (x -direction in Figure 6), the first VM of the structure (right image of Figure 6), its corresponding MDs, and the PSs associated with the shape parameters used in each different simulation. The selection of the shape variations, while not the focus of this first results section, is the same as the selection used in the shape optimization experiences described in Section 6.2 and Figure 10. In particular, the shape variations used in the optimization cases SO1, SO2, and SO3, use 3, 5 and 8 shape variations represented in Figure 10. We also consider cases without any shape parameter, denoted as ROM (in comparison to PROM).

We show that the ROM constructed with the selected ROB is accurate by comparing it to alternative ROB selections (Section C.2).

6.1.3 Solver parameters In order to solve the EoMs (1) and (13), several numerical parameters need to be specified. The EoMs are solved using the Newmark- β integration scheme (Géradin and Rixen 2015), with a time step of 0.02 s and a horizon of 2 s. The sensitivity (19) is computed without solving a separate ODE, but equivalently by using the Jacobian of the EoMs and computing the residual with respect to the optimization parameters, following Brüls and Eberhard (2008). The optimization horizon of the cost function (17) is set to the last 0.1 s ($n = 96$, $N = 101$).

We set the density of the fluid to $\rho = 1000 \text{ kg/m}^3$. The actuation signals applied to the muscle elements shown in Figure 6 are opposite sinusoids with a frequency of 1 Hz and an amplitude $a = 0.2$. The actuation stiffness k varies between experiments, affecting the overall oscillation of the tail. We choose these simple-to-model signals because the focus of this work is shape optimization, and discuss limitations and future developments for actuation optimization in Section 7. First results in that direction are presented in Section 6.3.

6.1.4 Model comparisons To compare the FOM, ROM, and PROM formulations, we simulate these models for five different mesh discretizations (between 1272 and 24822

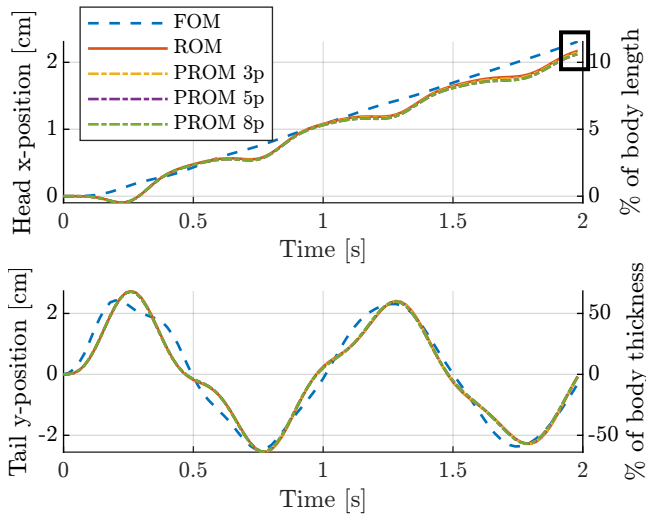


Figure 7. Comparison of the solutions obtained by simulating the FOM, ROM, and PROM for multiple share variation parameters (3,5, and 8 parameters), for a mesh discretized in 8086 FEs and an actuation amplitude of $k = 8.5 \cdot 10^4$. The upper panel shows the swimming distance achieved by the fish (head position along the x -direction), and the lower panel shows the oscillation of the tail (y -position) across time. The error between the FOM and (P)ROMs after 2 s (rectangle in the upper panel) is reported in Figure 8.

FEs), and multiple actuation stiffnesses k (between $1.9 \cdot 10^4$ and $14.5 \cdot 10^4$), resulting in different amplitudes of the tail oscillation. For each combination of mesh discretization and actuation stiffness, we compare the solution obtained by simulating the ROM and PROM to the solution obtained by simulating the FOM. In particular, we focus on the head position in the swimming direction (x -position) and the tail position in the oscillation direction (y -position), as shown in Figure 7 for the example of a mesh discretization of 8086 elements and an actuation stiffness of $k = 8.5 \cdot 10^4$. Because the ROB used by the different PROMs is similar to the one used by the ROM (with the additional basis vectors contained in the matrix Ξ), their simulation results for the nominal shape are the same. Compared to the FOM, all (P)ROMs yield a smaller swimming distance (Figure 7, upper panel), due to their inability to fully capture the full oscillation of the tail (Figure 7, lower panel). Specifically, the relative error in the swimming distance between the FOM and the (P)ROM is -6% percent after 2 s (see rectangle in Figure 7).

To compare the models more globally, we repeat the analysis of Figure 7 for multiple combinations of mesh discretization and oscillation amplitudes. The results are shown in Figure 8. As an example, the relative error reported for the case presented in Figure 7 is highlighted by a rectangle in both figures. The relative error remains small for most combinations (between -10% and +15%), and in particular for an amplitude of around 2cm, where we operate the system in Section 6.2. While the relative error grows for small oscillation amplitudes, the absolute error decreases (Figure 16). The accuracy of the (P)ROMs is strengthened by the fact that other choices of muscle placements also lead to a meaningful error profile (Figure 18), and the solver operates in a regime of convergence under the chosen time step (Section C.3)

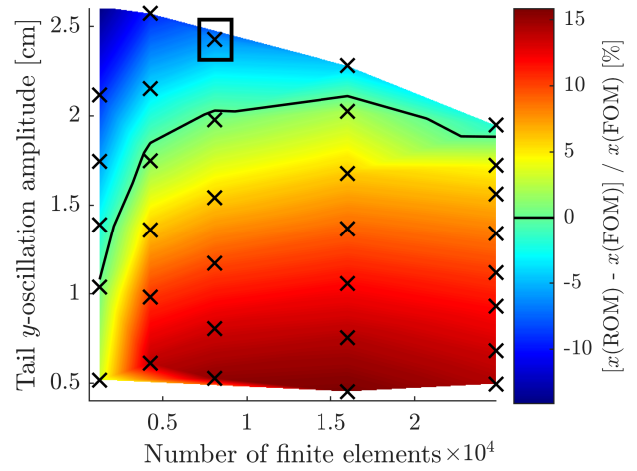


Figure 8. Relative error in the swimming distance after $t = 2$ s between the FOM and the ROM for multiple discretizations and oscillation's amplitudes of the nominal shape (see Figure 6). The crosses indicate simulations results, and the heat map is obtained using a linear interpolation between these results. Simulations of the FOM performed in the white area in the top right corner (i.e., for large number of FEs and large oscillations) did not converge. The rectangle corresponds to the relative error measured in Figure 7.

While simulation results of (P)ROMs are similar to those obtained with the FOM, they require significantly less computation efforts. Panel (A) of Figure 9 shows the simulation time required to solve the EoMs for the different models and mesh discretizations, averaged over the different oscillation amplitudes of Figure 8. As can be expected, the simulation time increases with the number of FEs. Comparing the different models, the time required by the ROM is approximately one order of magnitude smaller compared to the time required by the FOM. The simulation of the different PROMs requires more computational effort than the ROM because of their enhanced ROB. This computational effort increases with the number of parameters used to describe the shape variations.

Panels (B) and (C) of Figure 9 split the computation effort of the ROM and the PROM with 3 parameters into two parts: the time needed to build the model (i.e., to construct the reduced order tensors) and the time needed to solve the EoMs. For both cases, the total computation effort is driven by the model building, which increases with the number of FEs, while the time needed to simulate the system, i.e., to solve the EoMs, is constant for the different discretization. This pattern is explained by the fact that the reduced order tensors are constructed by considering the contribution of each FE, but the dimensionality of the EoMs (13) is independent of the mesh discretization. While the PROMs require more computational resources compared to the ROM, they allow the computation of analytical sensitivities, which are leveraged in the optimization pipeline introduced in Section 5, whose performance is analyzed next.

6.2 Shape optimization

We now turn to the shape optimization (SO) of soft swimmers, using the pipeline shown in Figure 5. Starting

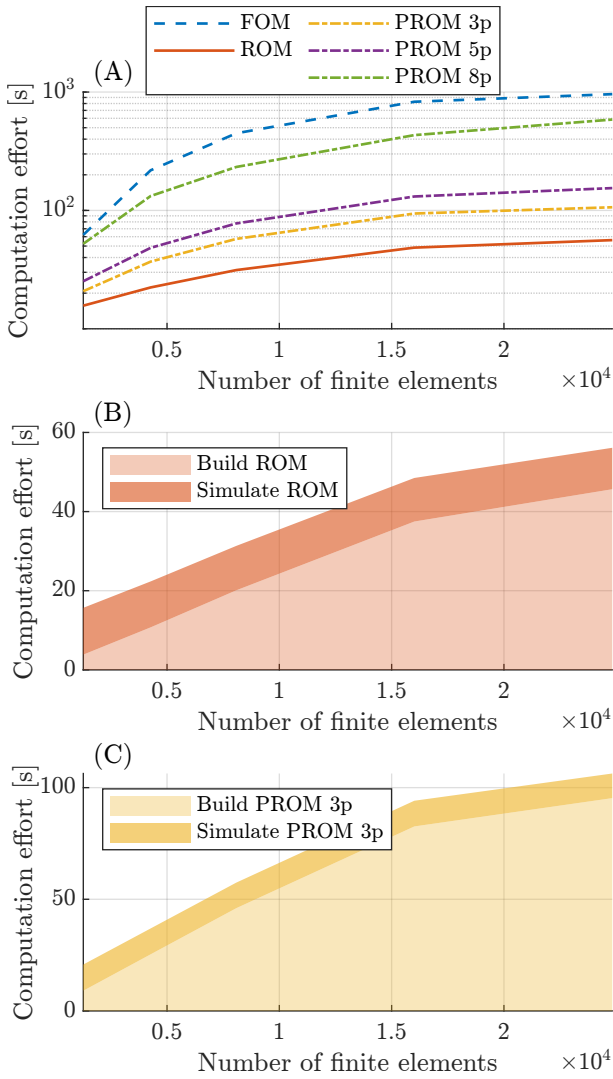


Figure 9. Computation effort as a function of the number of finite elements, for different models. Panel (A) shows the total computation effort for the FOM, ROM and 3 PROMs with respectively 3, 5, and 8 parameters. Panels (B) and (C) decompose the cost for the ROM and the PROM with 3 parameters into the time needed to build the model and the time needed to simulate it.

from a uniform 3-dimensional block (Figure 6), our goal is to find an optimal shape that maximizes the distance traveled in x -direction by the fish within a 2 seconds time horizon. We present 6 primary numerical experiments, summarized in Table 1. These experiments differ in the discretization of the mesh and in the number of optimization parameters. The optimization parameters correspond to different shape variations, which can be linearly combined to find the final optimal shape (overview in Figure 10). After presenting the results of these 6 experiments (Sections 6.2.1 to 6.2.4), we discuss robustness checks and additional results in Section 6.2.5. Finally, Section 6.2.6 discusses comparisons to other non-gradient based optimization strategies.

6.2.1 Experiment SO1 \otimes The search space of the first experiment SO1 is composed of the 3 shape variations presented in the upper row of Figure 10. Therefore, the parameter vector ξ contains 3 parameters. We assign the following constraints to the parameters: $-0.5 \leq \xi_1, \xi_2 \leq 0.5$

and $-0.15 \leq \xi_3 \leq 0.15$. These constraints are summarized in Table 2.

The obtained optimal shape is depicted in Figure 11. As could be intuitively expected, this simple example shows the creation of a thinner fish with a tail and a head, therefore maximizing its propulsion. The optimal fish traveled a distance 3.8 larger than the nominal fish (Figure 14).

This numerical case study is fast to solve, as reported in Table 1. It took 5.74 min to converge and required 6 rebuilds of the PROM and resolving of the EoMs (see Figure 5), leading to an average of 0.96 min per build and EoMs solve.

6.2.2 Experiment SO2 \oplus In this experiment, we augment the search space of SO1 replacing the shape ξ_3 by the three shape variations in the second row of Figure 10, for a total of 5 search parameters. Similarly to SO1, the optimal shape (Figure 12) allows to outperform the nominal shape by a factor of 5.60 (Figure 14). Because of the larger search space, SO2 requires slightly more computational effort than SO1 and converges in 7.86 min (1.31 min per build and EoMs solve).

6.2.3 Experiment SO3 \odot The numerical experiment SO3, which includes 8 parameters as shown in Figure 10, results in the optimal shape Figure 13. Compared to SO1 and SO2, the optimal shape is characterized by a more slender forebody and an enlarged tail, given the smaller body size. This optimal shape allows us to outperform the nominal shape by a factor 8 and the optimal shapes obtained in SO1 and SO2 as shown in Figure 14. In terms of computational effort, SO3 converges in 12.6 min, which is fast but slower than SO1 (factor of 3.2) and SO2 (factor of 2.3) due to the larger number of search parameters.

6.2.4 Experiments SO4 to SO6 To assess the properties of our method for finer meshes, we re-run the experiments SO1 to SO3 using a finer FE mesh. The main characteristics of these case studies are reported in Table 1. The optimal shapes are identical to those of SO1-SO3 within the numerical accuracy limits of our pipeline and therefore are not explicitly shown. Because of the finer mesh discretization, the optimization requires more time to run (approximately a factor 3 compared to SO1-SO3), an increase which is mainly driven by the additional time required to build the PROMs (see Figure 9).

6.2.5 Robustness checks We run multiple robustness checks that we report in Section C. The key insights from these additional results are the following:

- The obtained optimal parameters are likely to represent global optima. Different parameter initializations leads to the same optimal values (Section D.1).
- The solution approximations based on the PROM sensitivities (21) used in the optimization pipeline represent a trade-off. Using the gradient computed based on these approximations allows to avoid rebuilding a PROM, but it might not be accurate. In the cases we consider, the descent direction remains precise in the interval between two PROM builds (Section D.2).

Table 1. Summary of the numerical case studies. The column “# Build & EoMs” reports the number of times the PROM was built and the EoMs solved, according to the algorithm presented in Figure 5. Accordingly, the far-right column reports the average time needed to build the PROM and solve the EoMs once, i.e., for one outer loop iteration of the algorithm.

Case	# Parameters	# FEs	# DoFs FOM	# DoFs PROM	# Build & EoMs	Time [min.]	Time/(Build & EoMs) [min.]
SO1	3	8086	5181	6	6	5.74	0.96
SO2	5	8086	5181	8	6	7.86	1.31
SO3	8	8086	5181	11	6	22.34	3.72
SO4	3	16009	9714	6	5	14.11	2.82
SO5	5	16009	9714	8	6	21.90	3.65
SO6	8	16009	9714	11	6	68.59	11.43

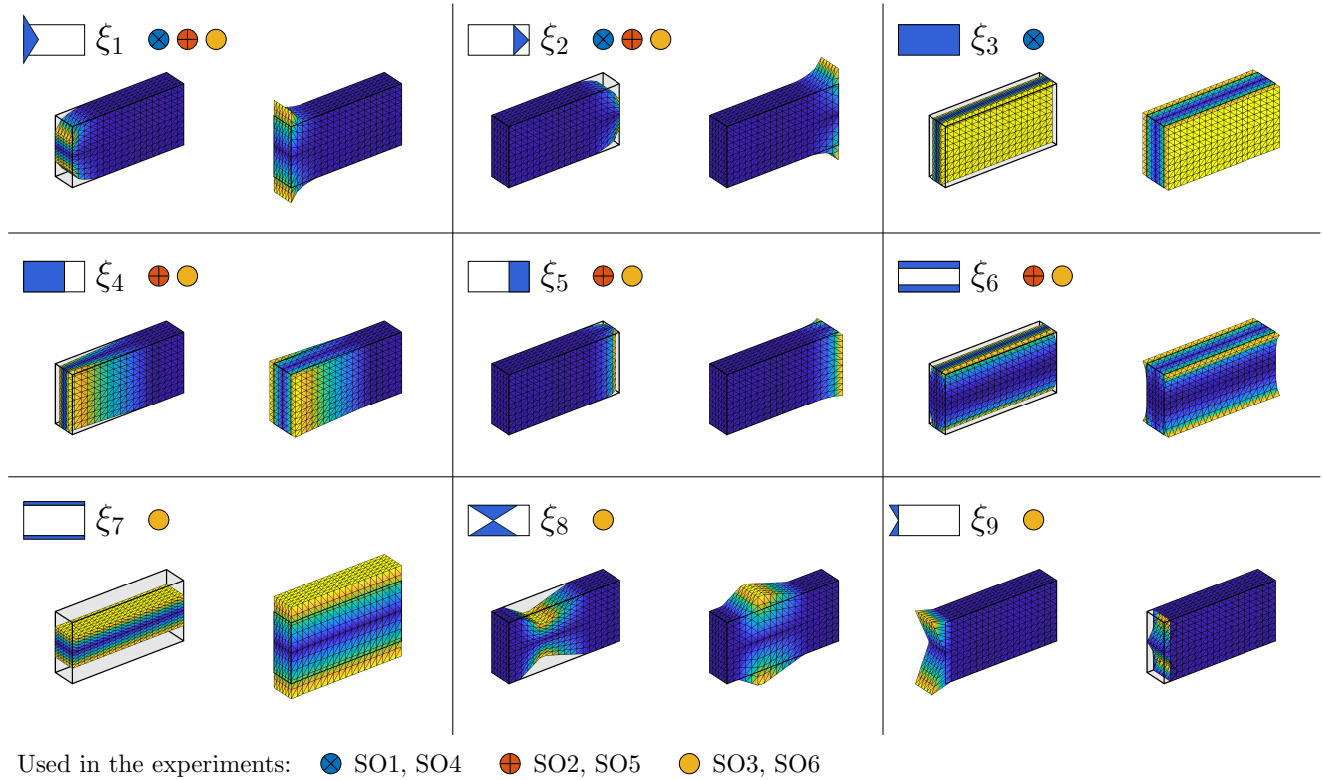


Figure 10. Shape variations used in the different numerical experiments. Each panel corresponds to a different shape variation obtained using the method described in Section 4.1 and Figure 4, i.e., a single column of U . In each panel, the i -th column of U is multiplied by $\xi_i = 0.5$ (left shape), and $\xi_i = -0.5$ (right shape). The numerical experiments combine the shape variations according to the round symbols to build the matrix U , e.g., SO1 uses the shape variations $i = 1, 2, 3$ to obtain $U \in \mathbb{R}^{n \times 3}$.

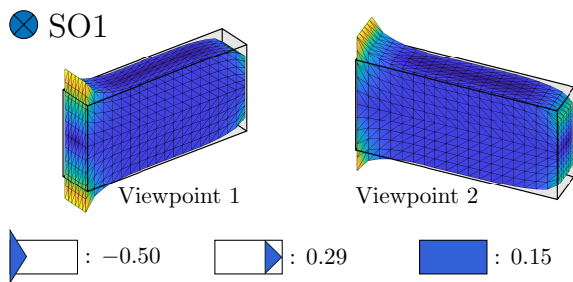


Figure 11. Optimal shape obtained for SO1, presented from two different viewpoints. The symbols and their values correspond to the optimal parameters obtained for each shape variation of the search space (Figure 10).

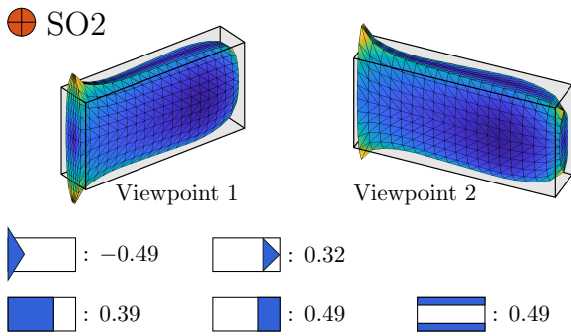
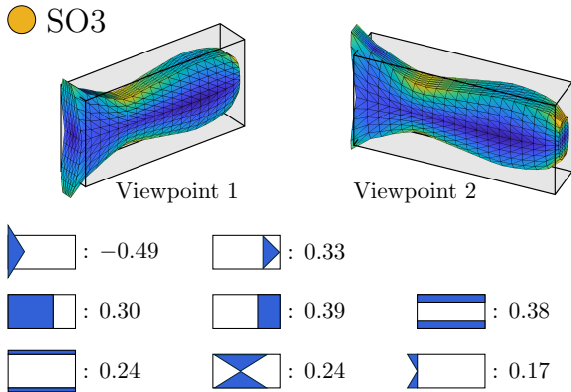
- The quality of the design search space ultimately depends on the expressiveness of not only the single shape variations, but also their linear combinations. The optimization pipeline allows practitioners to rapidly test different designs of a specific morphological feature (e.g., the fish tail) while respecting manufacturing constraints (Section D.3).

6.2.6 Discussion and comparison The results presented above show that the PROM-based optimization reliably finds optima in the search space, and is especially fast for up to approximately 5 parameters. The PROM sensitivities allow to compute gradient of the cost function and therefore efficiently search the parameter space.

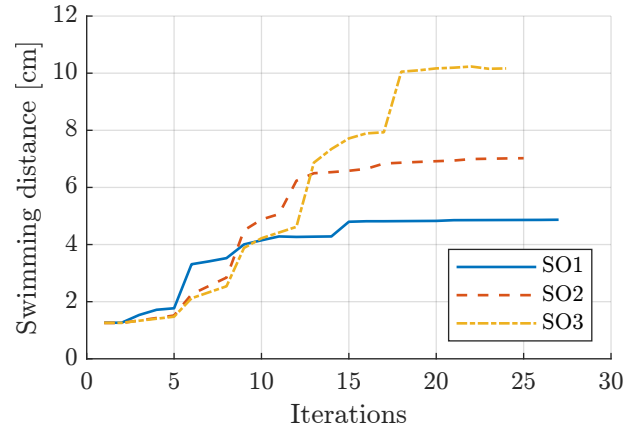
The efficiency of the PROM-based approach is particularly clear when compared to the potential for a FOM- or ROM-based algorithms. The FOM is significantly more

Table 2. Lower and upper bound on the search parameters for the different shape optimization experiments.

Case	SO1, SO4	SO2, SO5	SO3, SO6
ξ_1	-0.5, 0.5	-0.5, 0.5	-0.5, 0.5
ξ_2	-0.5, 0.5	-0.5, 0.5	-0.5, 0.5
ξ_3	-0.15, 0.15	not used	not used
ξ_4	not used	-0.4, 0.4	-0.3, 0.3
ξ_5	not used	-0.5, 0.5	-0.4, 0.4
ξ_6	not used	-0.5, 0.5	-0.4, 0.4
ξ_7	not used	not used	-0.25, 0.25
ξ_8	not used	not used	-0.25, 0.25
ξ_9	not used	not used	-0.01, 0.2

**Figure 12.** Optimal shape obtained for SO2, presented from two different viewpoints. The symbols and their values correspond to the optimal parameters obtained for each shape variation of the search space (Figure 10).**Figure 13.** Optimal shape obtained for SO3, presented from two different viewpoints. The symbols and their values correspond to the optimal parameters obtained for each shape variation of the search space (Figure 10).

costly to run (Figure 9) and does not provide analytical sensitivities with respect to the shape parameters. An alternative would be to consider the ROM and perform a grid search without gradient. However, this is way less efficient than the PROM-based method: Table 3 shows that for a similar granularity of the search space as the rebuild threshold of the PROM-based algorithm, a ROM grid search would suffer from the curse of dimensionality with few parameters

**Figure 14.** Swimming distance across optimization iterations. After convergence, the optimal shapes obtained in the experiments SO1, SO2, and SO3 clearly outperform the nominal shape. The optimal shape obtained with SO3 allows for larger swimming distance compared to SO2 and SO1, although the difference is relatively small.**Table 3.** Computational effort estimation for a ROM-based grid search. The time per ROM solve is taken from Section 6.1.4.

Case	SO1	SO2	SO3
Number of parameters	3	5	8
Number of corners	8	32	256
Number of combinations	147	14406	367500
Single ROM solve time [s]	31	31	31
Time for corners only [min]	4.1	16.5	132
Time for all combi. [h]	1.26	124	3165
Time for PROM [min]	5.7	7.86	22.3

already. Even when solving for the corners of the search hyperbox, a ROM-based model is slower in most cases. These results confirm the appropriateness of the proposed optimization scheme.

6.3 Multi-objective co-optimization

We illustrate how the shape optimization pipeline can be extended to a multi-objective, co-optimization framework by focusing on two competing objectives: a large swimming distance and a low energy use. To describe the energy use, we parametrize the sinusoidal actuation signal by its amplitude a and consider the following quadratic actuation energy:

$$L_{\text{energy}} = \alpha a^2, \quad (22)$$

where α is a constant. The resulting multi-objective cost function is

$$L = w_1 L_{\text{distance}} + w_2 L_{\text{energy}}, \quad (23)$$

where L_{distance} is the cost from the swimming distance (17), and w_1, w_2 are weights such that $w_1 + w_2 = 1$.

The computation of the analytical sensitivities (19) needed to perform co-optimization of the shape and actuation signal is straightforward, as the actuation parameter (i.e., the signal amplitude) affects the EoMs exclusively through the actuation force (12). Concretely, this implies that the partial

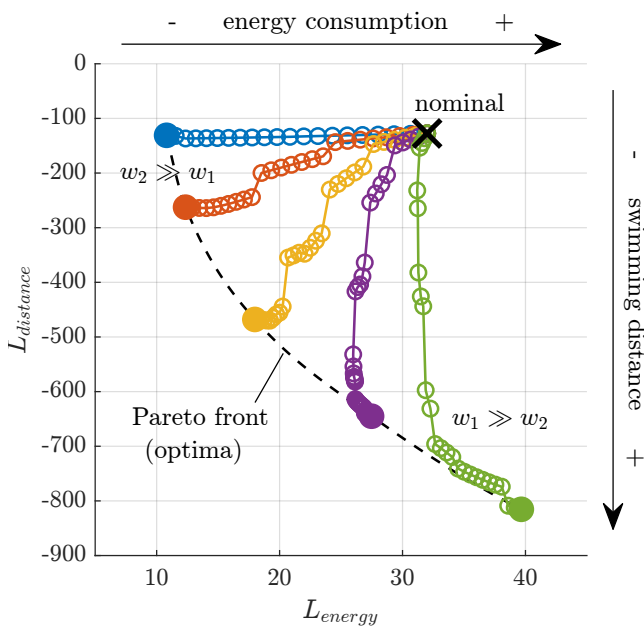


Figure 15. Multi-objective co-optimization results. Depending on the weights w_1 and w_2 , different trade-off between energy consumption and swimming distance are achieved. Filled circles represent optima, while empty circles represent parameters discovered during the optimization.

derivatives of all other forces with respect to the actuation parameter vanish. In contrast, the partial derivatives of the actuation force with respect to the shape parameters must be augmented by its derivative with respect to the actuation parameter. The same reasoning extends to more complex actuation parametrizations.

We illustrate the multi-objective co-optimization in Figure 15, where we use the shape variations of SO2 (total of 6 parameters) and vary the weights w_1 and w_2 . When $w_2 \gg w_1$, solutions with smaller actuation amplitudes are found, thereby reducing energy consumption. Conversely, when $w_1 \gg w_2$, the optimization prioritizes achieving greater swimming distance. The set of optimal trade-offs forms a Pareto front shown in Figure 15.

While the actuation amplitude varies as expected at the different Pareto optima, the optimal fish morphology is barely affected. This is due to the fact that the energy cost L_{energy} is not a function of the fish shape, as the energy per muscle element is computed based on the nominal shape and not updated during optimization (Section 3.5). The only parameter explicitly coupling the two objectives is the actuation amplitude.

This simple example illustrates that the shape optimization pipeline developed in this work can accommodate the co-optimization of fish morphologies and actuation signals. A comprehensive treatment of optimal control strategies lies beyond the scope of the present study but present an exciting extension for future work, which we discuss next.

7 Conclusion and future work

In this paper, we presented a novel shape optimization pipeline for reduced order models of mechanical FEM structures subject to nonlinear forces. To showcase the capabilities of this approach, we applied it to the task

of finding optimal shapes of soft robotic fishes, which undergo large deformations and experience internal and external (hydrodynamic) nonlinear forces. We first validated the developed parametric reduced order models (PROMs) against full order models (FOMs) in terms of accuracy and computational effort. We then leveraged these accurate and computationally efficient PROMs, and in particular their corresponding parameter sensitivities, to perform gradient-based optimization. The resulting optimal shapes outperform the nominal shape by factors up to 8 and are obtained rapidly (within a few minutes, see Table 1), making the presented methodology well suited for fast, physics-based design optimization.

The optimization pipeline developed in this paper shows, however, a few limitations. Although the accuracy of the PROMs was validated against FOMs, we did not compare our results against real-world robotic systems or more advanced hydrodynamic models. Instead, we relied on previous works that employed or assessed the Lighthill's hydrodynamic model (Wang et al. 2011; Li et al. 2014; Ma et al. 2021b; Eloy and Michelin 2024). Validating the optimal fish shapes against physical robotic prototypes is a promising direction for future work, which would allow assessing existing sim-to-real gaps (Dubied et al. 2022). Such comparisons would also clarify whether extending the reduction of internal forces used by Marconi et al. (2021) to more advanced formulations – such as co-rotational or Neo-Hookean constitutive models – would meaningfully improve the fidelity of the PROM solutions.

Importantly, our work advances existing methods using PROMs for optimization (Fröhlich et al. 2019) by incorporating nonlinear forces into the optimization pipeline. Future work should also consider the use of this general PROM-based optimization method to other scenarios, and in particular to standard scenarios for which optimization can easily be performed using off-the-shelf optimizers, allowing for a thorough comparison. Finally, a more detailed treatment of richer actuation signals within co-optimization settings (Section 6.3) could enable more practically relevant applications.

Altogether, the optimization method presented in this paper shows how nonlinear PROMs can be used for optimization tasks in a computationally efficient way, unlocking new opportunities for more efficient robotic design and control.

References

- Armanini C, Alshehhi AA, Mathew AT, Hmida IB, Stefanini C and Renda F (2022) Model-based design optimization of underwater flagellate propellers. *IEEE Robotics and Automation Letters* 7(4): 10089–10096.
- Bächer M, Knoop E and Schumacher C (2021) Design and Control of Soft Robots Using Differentiable Simulation. *Current Robotics Reports* 2:2 2(2): 211–221.
- Bern JM, Banzet P, Poranne R and Coros S (2019) Trajectory optimization for cable-driven soft robot locomotion. In: *Robotics: Science and Systems*, volume 1.
- Bruder D, Bombara D and Wood RJ (2025) A koopman-based residual modeling approach for the control of a soft robot arm. *The International journal of robotics research* 44(3): 388–406.

- Bruder D, Gillespie B, Remy CD and Vasudevan R (2019) Modeling and control of soft robots using the koopman operator and model predictive control. *arXiv preprint arXiv:1902.02827*.
- Brüls O and Eberhard P (2008) Sensitivity analysis for dynamic mechanical systems with finite rotations. *International Journal for Numerical Methods in Engineering* 74(13): 1897–1927.
- Candelier F, Boyer F and Leroyer A (2011) Three-dimensional extension of lighthill’s large-amplitude elongated-body theory of fish locomotion. *Journal of Fluid Mechanics* 674: 196–226.
- Candelier F, Porez M and Boyer F (2013) Note on the swimming of an elongated body in a non-uniform flow. *Journal of Fluid Mechanics* 716: 616–637.
- Chen F, Song Z, Chen S, Gu G and Zhu X (2023a) Morphological design for pneumatic soft actuators and robots with desired deformation behavior. *IEEE Transactions on Robotics* 39(6): 4408–4428.
- Chen Z, Tian X, Chen X, Wen B and Li X (2023b) An experimental study of the wire-driven compliant robotic fish. *Ocean Engineering* 279: 114433.
- Curatolo M and Teresi L (2015) The virtual aquarium: simulations of fish swimming. In: *Proc. European COMSOL Conference*.
- Della Santina C, Bicchi A and Rus D (2020a) On an improved state parametrization for soft robots with piecewise constant curvature and its use in model based control. *IEEE Robotics and Automation Letters* 5(2): 1001–1008.
- Della Santina C, Katzschmann RK, Bicchi A and Rus D (2020b) Model-based dynamic feedback control of a planar soft robot: trajectory tracking and interaction with the environment. *The International Journal of Robotics Research* 39(4): 490–513. DOI:10.1177/0278364919897292. URL <https://doi.org/10.1177/0278364919897292>.
- Du T, Hughes J, Wah S, Matusik W and Rus D (2021a) Underwater soft robot modeling and control with differentiable simulation. *IEEE Robotics and Automation Letters* 6(3): 4994–5001.
- Du T, Wu K, Ma P, Wah S, Spielberg A, Rus D and Matusik W (2021b) Diffpd: Differentiable projective dynamics. *ACM Trans. Graph.* 41(2).
- Dubied M, Michelis MY, Spielberg A and Katzschmann RK (2022) Sim-to-real for soft robots using differentiable fem: Recipes for meshing, damping, and actuation. *IEEE Robotics and Automation Letters* 7(2): 5015–5022.
- Duriez C (2013) Control of elastic soft robots based on real-time finite element method. In: *2013 IEEE international conference on robotics and automation*. IEEE, pp. 3982–3987.
- Duriez C, Coevoet E, Largilliere F, Morales-Bieze T, Zhang Z, Sanz-Lopez M, Carrez B, Marchal D, Goury O and Dequidt J (2016) Framework for online simulation of soft robots with optimization-based inverse model. In: *2016 IEEE International Conference on Simulation, Modeling, and Programming for Autonomous Robots (SIMPAR)*. pp. 111–118.
- Eloy C and Michelin S (2024) Flow associated with lighthill’s elongated-body theory. *arXiv preprint arXiv:2409.20162*.
- Frohlich B, Gade J, Geiger F, Bischoff M and Eberhard P (2019) Geometric element parameterization and parametric model order reduction in finite element based shape optimization. *Computational Mechanics* 63: 853–868.
- Geilinger M, Hahn D, Zehnder J, Bäcker M, Thomaszewski B and Coros S (2020) Add: Analytically differentiable dynamics for multi-body systems with frictional contact. *ACM Trans. Graph.* 39(6).
- Gérardin M and Rixen DJ (2015) *Mechanical vibrations: theory and application to structural dynamics*. John Wiley & Sons.
- Goury O, Carrez B and Duriez C (2021) Real-time simulation for control of soft robots with self-collisions using model order reduction for contact forces. *IEEE Robotics and Automation Letters* 6(2): 3752–3759.
- Goury O and Duriez C (2018) Fast, generic, and reliable control and simulation of soft robots using model order reduction. *IEEE Transactions on Robotics* 34(6): 1565–1576.
- Gravert SD, Michelis MY, Rogler S, Tscholl D, Buchner T and Katzschmann RK (2022) Planar modeling and sim-to-real of a tethered multimaterial soft swimmer driven by peano-hasels. In: *2022 IEEE/RSJ International Conference on Intelligent Robots and Systems (IROS)*. IEEE, pp. 9417–9423.
- Gravert SD, Varini E, Kazemipour A, Michelis MY, Buchner T, Hinchet R and Katzschmann RK (2024) Low-voltage electrohydraulic actuators for untethered robotics. *Science Advances* 10(1): eadi9319. DOI:10.1126/sciadv.adi9319. URL <https://www.science.org/doi/10.1126/sciadv.adi9319>.
- Hahn D, Banzet P, Bern JM and Coros S (2019) Real2Sim: viscoelastic parameter estimation from dynamic motion. *ACM Transactions on Graphics* 38(6): 1–13. DOI:10.1145/3355089.3356548. URL <https://dl.acm.org/doi/10.1145/3355089.3356548>.
- Holsten F, Engell-Nørregård MP, Darkner S and Erleben K (2019) Data driven inverse kinematics of soft robots using local models. In: *2019 International Conference on Robotics and Automation (ICRA)*. IEEE, pp. 6251–6257.
- Hu Y, Anderson L, Li TM, Sun Q, Carr N, Ragan-Kelley J and Durand F (2020) DiffTaichi: Differentiable Programming for Physical Simulation. DOI:10.48550/arXiv.1910.00935. URL <http://arxiv.org/abs/1910.00935>. ArXiv:1910.00935 [physics, stat].
- Hu Y, Liu J, Spielberg A, Tenenbaum JB, Freeman WT, Wu J, Rus D and Matusik W (2019) Chainqueen: A real-time differentiable physical simulator for soft robotics. In: *2019 International Conference on Robotics and Automation (ICRA)*. pp. 6265–6271.
- Huang X, Rong Y and Gu G (2024) High-precision dynamic control of soft robots with the physics-learning hybrid modeling approach. *IEEE/ASME Transactions on Mechatronics*.
- Huang Z, Hu Y, Du T, Zhou S, Su H, Tenenbaum JB and Gan C (2021) PlasticineLab: A Soft-Body Manipulation Benchmark with Differentiable Physics. DOI:10.48550/arXiv.2104.03311. URL <http://arxiv.org/abs/2104.03311>. ArXiv:2104.03311 [cs].
- Jain S, Marconi J and Tiso P (2022) Yetanotherfemcode. DOI: 10.5281/zenodo.7313486. URL <https://doi.org/10.5281/zenodo.7313486>.
- Jain S, Tiso P, Rutzmoser JB and Rixen DJ (2017) A quadratic manifold for model order reduction of nonlinear structural dynamics. *Computers & Structures* 188: 80–94.
- Karamooz Mahdiabadi M, Bartl A, Xu D, Tiso P and Rixen DJ (2019) An augmented free-interface-based modal substructuring for nonlinear structural dynamics including interface reduction. *Journal of Sound and Vibration* 462: 114915. DOI:<https://doi.org/10.1016/j.jsv.2019.114915>. URL <https://www.sciencedirect.com/science/>

[article/pii/S0022460X19304778](https://doi.org/10.1007/978-3-319-23778-7_27).

- Katzschmann RK, DelPreto J, MacCurdy R and Rus D (2018) Exploration of underwater life with an acoustically controlled soft robotic fish. *Science Robotics* 3(16): eaar3449.
- Katzschmann RK, Marchese AD and Rus D (2016) Hydraulic Autonomous Soft Robotic Fish for 3D Swimming. In: Hsieh MA, Khatib O and Kumar V (eds.) *Experimental Robotics: The 14th International Symposium on Experimental Robotics*, Springer Tracts in Advanced Robotics. Cham: Springer International Publishing. ISBN 978-3-319-23778-7, pp. 405–420. DOI:10.1007/978-3-319-23778-7_27. URL https://doi.org/10.1007/978-3-319-23778-7_27.
- Katzschmann RK, Thieffry M, Goury O, Kruszewski A, Guerra TM, Duriez C and Rus D (2019a) Dynamically closed-loop controlled soft robotic arm using a reduced order finite element model with state observer. In: *2019 2nd IEEE International Conference on Soft Robotics (RoboSoft)*. pp. 717–724.
- Katzschmann RK, Thieffry M, Goury O, Kruszewski A, Guerra TM, Duriez C and Rus D (2019b) Dynamically closed-loop controlled soft robotic arm using a reduced order finite element model with state observer. In: *2019 2nd IEEE international conference on soft robotics (RoboSoft)*. IEEE, pp. 717–724.
- Laschi C, Cianchetti M, Mazzolai B, Margheri L, Follador M and Dario P (2012) Soft robot arm inspired by the octopus. *Advanced robotics* 26(7): 709–727.
- Li L, Wang C and Xie G (2014) Modeling of a carangiform-like robotic fish for both forward and backward swimming: Based on the fixed point. In: *2014 IEEE International Conference on Robotics and Automation (ICRA)*. IEEE, pp. 800–805.
- Lighthill MJ (1971) Large-amplitude elongated-body theory of fish locomotion. *Proceedings of the Royal Society of London. Series B. Biological Sciences* 179(1055): 125–138.
- Liu S, Liu C, Wei G, Ren L and Ren L (2025) Design, modeling, and optimization of hydraulically powered double-joint soft robotic fish. *IEEE Transactions on Robotics* .
- Liu W, Bai K, He X, Song S, Zheng C and Liu X (2022) Fishgym: A high-performance physics-based simulation framework for underwater robot learning. In: *2022 International Conference on Robotics and Automation (ICRA)*. IEEE, pp. 6268–6275.
- Ma P, Du T, Zhang JZ, Wu K, Spielberg A, Katzschmann RK and Matusik W (2021a) Diffaqua: A differentiable computational design pipeline for soft underwater swimmers with shape interpolation. *ACM Trans. Graph.* 40(4).
- Ma P, Du T, Zhang JZ, Wu K, Spielberg A, Katzschmann RK and Matusik W (2021b) DiffAqua: A Differentiable Computational Design Pipeline for Soft Underwater Swimmers with Shape Interpolation. In: *arXiv:2104.00837 [cs]*. URL <http://arxiv.org/abs/2104.00837>. ArXiv: 2104.00837.
- Marconi J, Tiso P and Braghin F (2020) A nonlinear reduced order model with parametrized shape defects. *Computer Methods in Applied Mechanics and Engineering* 360: 112785.
- Marconi J, Tiso P, Quadrelli DE and Braghin F (2021) A higher-order parametric nonlinear reduced-order model for imperfect structures using Neumann expansion. *Nonlinear Dynamics* 104(4): 3039–3063.
- Matthews D, Spielberg A, Rus D, Kriegman S and Bongard J (2023) Efficient automatic design of robots. *Proceedings of the National Academy of Sciences* 120(41): e2305180120.
- Min S, Won J, Lee S, Park J and Lee J (2019) Softcon: Simulation and control of soft-bodied animals with biomimetic actuators. *ACM Trans. Graph.* 38(6).
- Nava E, Zhang JZ, Michelis MY, Du T, Ma P, Grewe BF, Matusik W and Katzschmann RK (2022) Fast aquatic swimmer optimization with differentiable projective dynamics and neural network hydrodynamic models. In: *International Conference on Machine Learning*. PMLR, pp. 16413–16427.
- Navez T, Ménager E, Chaillou P, Goury O, Kruszewski A and Duriez C (2025) Modeling, embedded control and design of soft robots using a learned condensed fem model. *IEEE Transactions on Robotics* .
- Pinskier J, Wang X, Liow L, Xie Y, Kumar P, Langelaar M and Howard D (2024) Diversity-based topology optimization of soft robotic grippers. *Advanced Intelligent Systems* 6(4): 2300505.
- Qin L, Peng H, Huang X, Liu M and Huang W (2024) Modeling and simulation of dynamics in soft robotics: A review of numerical approaches. *Current Robotics Reports* 5(1): 1–13.
- Reinhart RF and Steil JJ (2016) Hybrid mechanical and data-driven modeling improves inverse kinematic control of a soft robot. *Procedia Technology* 26: 12–19.
- Saccani A, Marconi J and Tiso P (2022) Sensitivity analysis of nonlinear frequency response of defected structures. *Nonlinear Dynamics* : 1–25.
- Shelton RM, Thornycroft PJ and Lauder GV (2014) Undulatory locomotion of flexible foils as biomimetic models for understanding fish propulsion. *Journal of Experimental Biology* 217(12): 2110–2120.
- Spielberg A, Araki B, Sung C, Tedrake R and Rus D (2017) Functional co-optimization of articulated robots. In: *2017 IEEE International Conference on Robotics and Automation (ICRA)*. IEEE, pp. 5035–5042.
- Tawk C and Alici G (2020) Finite element modeling in the design process of 3d printed pneumatic soft actuators and sensors. *Robotics* 9(3): 52.
- Tiso P, Dedden R and Rixen DJ (2013) A modified discrete empirical interpolation method for reducing non-linear structural finite element models. In: *Proceedings of the ASME 2013 International Design Engineering Technical Conferences and Computers and Information in Engineering Conference, 9th International Conference on Multibody Systems, Nonlinear Dynamics, and Control*, volume 7B. Portland, Oregon, USA: ASME, p. V07BT10A043. DOI:10.1115/DETC2013-13280. URL <https://doi.org/10.1115/DETC2013-13280>.
- Trivedi D, Dienno D and Rahn CD (2008a) Optimal, model-based design of soft robotic manipulators. *Journal of Mechanical Design* .
- Trivedi D, Lotfi A and Rahn CD (2008b) Geometrically exact models for soft robotic manipulators. *IEEE Transactions on Robotics* 24(4): 773–780.
- van den Berg SC, Scharff RBN, Rusák Z and Wu J (2020) Biomimetic Design of a Soft Robotic Fish for High Speed Locomotion. In: Vouloutsi V, Mura A, Tauber F, Speck T, Prescott TJ and Verschure PFMJ (eds.) *Biomimetic and Biohybrid Systems*, Lecture Notes in Computer Science. Cham: Springer International Publishing. ISBN 978-3-030-64313-3, pp. 366–377. DOI:10.1007/978-3-030-64313-3_35.
- Wandel N, Weinmann M and Klein R (2020) Learning incompressible fluid dynamics from scratch—towards fast, differentiable fluid models that generalize. *arXiv preprint*

arXiv:2006.08762 .

Wang J, Alequin-Ramos F and Tan X (2011) Dynamic modeling of robotic fish and its experimental validation. In: *2011 IEEE/RSJ International Conference on Intelligent Robots and Systems*. IEEE, pp. 588–594.

Wang J, Baiyinbaoligao, Mu X, Qie Z, Xu F and Li X (2024a) A novel spatial–temporal prediction method for the effects of fish movement on flow field based on hybrid deep neural network. *Engineering Applications of Computational Fluid Mechanics* 18(1): 2370927.

Wang R, Zhang C, Zhang Y, Yang L, Tan W, Qin H, Wang F and Liu L (2024b) Fast-swimming soft robotic fish actuated by bionic muscle. *Soft Robotics* 11(5): 845–856.

Wang X, Wang B, Pinskiar J, Xie Y, Brett J, Scalzo R and Howard D (2024c) Fin-bayes: A multi-objective bayesian optimization framework for soft robotic fingers. *Soft Robotics* 11(5): 791–801.

Webster III RJ and Jones BA (2010) Design and kinematic modeling of constant curvature continuum robots: A review. *The International Journal of Robotics Research* 29(13): 1661–1683.

Wu L and Tiso P (2016) Nonlinear model order reduction for flexible multibody dynamics: a modal derivatives approach. *Multibody System Dynamics* 36(4): 405–425. DOI:10.1007/s11044-015-9476-5. URL <https://doi.org/10.1007/s11044-015-9476-5>.

Wu L, Tiso P, Tatsis K and Rixen DJ (2019) A modal derivatives enhanced rubin substructuring method for geometrically nonlinear multibody systems. *Multibody System Dynamics* 45: 57–85. DOI:10.1007/s11044-018-09644-2. URL <https://doi.org/10.1007/s11044-018-09644-2>.

Zhang JZ, Zhang Y, Ma P, Nava E, Du T, Arm P, Matusik W and Katzschmann RK (2022) Sim2real for soft robotic fish via differentiable simulation. In: *2022 IEEE/RSJ International Conference on Intelligent Robots and Systems (IROS)*. IEEE, pp. 12598–12605.

Zhu J, White C, Wainwright DK, Santo VD, Lauder GV and Bart-Smith H (2019) Tuna robotics: A high-frequency experimental platform exploring the performance space of swimming fishes. *Science Robotics* 4(34). DOI:10.1126/scirobotics.aax4615. URL <https://robotics.sciencemag.org/content/4/34/eaax4615>. Publisher: Science Robotics Section: Research Article.

A Actuation force: matrices and tensors

In this section, we detail the expressions of the mathematical objects used to construct the actuation forces (12) at the element-level (for 3D settings).

$$\mathbf{I}_V = [1, 1, 1, 0, 0, 0]^\top \quad (24)$$

$$\mathbf{H} = \begin{bmatrix} 1 & 0 & 0 & 0 & 0 & 0 & 0 & 0 & 0 \\ 0 & 0 & 0 & 0 & 1 & 0 & 0 & 0 & 0 \\ 0 & 0 & 0 & 0 & 0 & 0 & 0 & 0 & 1 \\ 0 & 1 & 0 & 1 & 0 & 0 & 0 & 0 & 0 \\ 0 & 0 & 1 & 0 & 0 & 0 & 1 & 0 & 0 \\ 0 & 0 & 0 & 0 & 0 & 1 & 0 & 1 & 0 \end{bmatrix} \quad (25)$$

$$\mathbf{A}_1(\boldsymbol{\theta}) = \begin{bmatrix} u_{,x} & 0 & 0 & v_{,x} & 0 & 0 & w_{,x} & 0 & 0 \\ 0 & u_{,y} & 0 & 0 & v_{,y} & 0 & 0 & w_{,y} & 0 \\ 0 & 0 & u_{,z} & 0 & 0 & v_{,z} & 0 & 0 & w_{,z} \\ u_{,y} & u_{,x} & 0 & v_{,y} & v_{,x} & 0 & w_{,y} & w_{,x} & 0 \\ u_{,z} & 0 & u_{,x} & v_{,z} & 0 & v_{,x} & w_{,z} & 0 & w_{,x} \\ 0 & u_{,z} & u_{,y} & 0 & v_{,z} & v_{,y} & 0 & w_{,z} & w_{,y} \end{bmatrix} \quad (26)$$

(27)

\mathbf{L}_1 is a sparse third order tensor with elements $L_{ijk}^{(1)}$. Table 4 shows the non-zero element of this tensor.

Table 4. Non-zero elements of the \mathbf{L}_1 third order tensor (3D case).

$L_{111}^{(1)} = 1$	$L_{144}^{(1)} = 1$	$L_{177}^{(1)} = 1$	$L_{222}^{(1)} = 1$	$L_{255}^{(1)} = 1$
$L_{288}^{(1)} = 1$	$L_{333}^{(1)} = 1$	$L_{366}^{(1)} = 1$	$L_{399}^{(1)} = 1$	$L_{412}^{(1)} = 1$
$L_{421}^{(1)} = 1$	$L_{445}^{(1)} = 1$	$L_{454}^{(1)} = 1$	$L_{478}^{(1)} = 1$	$L_{487}^{(1)} = 1$
$L_{513}^{(1)} = 1$	$L_{531}^{(1)} = 1$	$L_{546}^{(1)} = 1$	$L_{564}^{(1)} = 1$	$L_{579}^{(1)} = 1$
$L_{597}^{(1)} = 1$	$L_{623}^{(1)} = 1$	$L_{632}^{(1)} = 1$	$L_{656}^{(1)} = 1$	$L_{665}^{(1)} = 1$
$L_{689}^{(1)} = 1$	$L_{698}^{(1)} = 1$			

B Reactive force: matrices and tensors

This section details the tensors present in (16). The reduced spine force at the element level is composed of three terms:

$$\mathbf{f}_I^r = {}^0\mathbf{f}_I^r + {}^1\mathbf{f}_I^r + {}^2\mathbf{f}_I^r$$

with

$$\begin{aligned} {}^0\mathbf{f}_I^r = & {}^{xx}T_{I_j}\ddot{\eta}_j + {}^{xU}T_{I_{jk}}\ddot{\eta}_j\xi_k + {}^{xV}T_{I_{jk}}\ddot{\eta}_j\eta_k \\ & + {}^{Ux}T_{I_{jk}}\ddot{\eta}_j\xi_k z_0 + {}^{UU}T_{I_{jkl}}\ddot{\eta}_j\xi_k\xi_l z_0 + {}^{UV}T_{I_{jkl}}\ddot{\eta}_j\xi_k\eta_l z_0 \\ & + {}^{Vx}T_{I_{jk}}\ddot{\eta}_j\eta_k + {}^{VU}T_{I_{jkl}}\ddot{\eta}_j\eta_k\xi_l + {}^{VV}T_{I_{jkl}}\ddot{\eta}_j\eta_k\eta_l \\ & + {}^{Vx}T_{I_{jk}}\dot{\eta}_j\dot{\eta}_k + {}^{VU}T_{I_{jkl}}\dot{\eta}_j\dot{\eta}_k\xi_l + {}^{VV}T_{I_{jkl}}\dot{\eta}_j\dot{\eta}_k\eta_l \\ & + {}^{xV}T_{I_{jk}}\dot{\eta}_j\dot{\eta}_k + {}^{UV}T_{I_{jkl}}\dot{\eta}_j\xi_k\dot{\eta}_l + {}^{VV}T_{I_{jkl}}\dot{\eta}_j\eta_k\dot{\eta}_l, \end{aligned}$$

$$\begin{aligned} {}^1\mathbf{f}_I^r = & {}^{xx}T_{I_{jk}}\dot{\eta}_j\xi_k + {}^{xU}T_{I_{jkl}}\dot{\eta}_j\xi_k\xi_l \\ & + {}^{xV}T_{I_{jkl}}\dot{\eta}_j\eta_k\xi_l + {}^{Ux}T_{I_{jkl}}\dot{\eta}_j\xi_k\xi_l \\ & + {}^{UU}T_{I_{jklm}}\dot{\eta}_j\xi_k\xi_l\xi_m + {}^{UV}T_{I_{jklm}}\dot{\eta}_j\xi_k\eta_l\xi_m \\ & + {}^{Vx}T_{I_{jkl}}\dot{\eta}_j\eta_k\xi_l + {}^{VU}T_{I_{jklm}}\dot{\eta}_j\eta_k\xi_l\xi_m \\ & + {}^{VV}T_{I_{jklm}}\dot{\eta}_j\eta_k\eta_l\xi_m + {}^{Vx}T_{I_{jkl}}\dot{\eta}_j\dot{\eta}_k\xi_l \\ & + {}^{VU}T_{I_{jklm}}\dot{\eta}_j\dot{\eta}_k\xi_l\xi_m + {}^{VV}T_{I_{jklm}}\dot{\eta}_j\dot{\eta}_k\eta_l\xi_m \\ & + {}^{xV}T_{I_{jkl}}\dot{\eta}_j\dot{\eta}_k\xi_l + {}^{UV}T_{I_{jklm}}\dot{\eta}_j\xi_k\dot{\eta}_l\xi_m \\ & + {}^{VV}T_{I_{jklm}}\dot{\eta}_j\eta_k\dot{\eta}_l\xi_m, \end{aligned}$$

$$\begin{aligned}
{}^2 f_I^T = & {}^{xx}T_{Ijkl} \ddot{\eta}_j \xi_k \xi_l & + & {}^{xU}T_{Ijklm} \ddot{\eta}_j \xi_k \xi_l \xi_m \\
& + {}^{xV}T_{Ijklm} \ddot{\eta}_j \eta_k \xi_l \xi_m & + & {}^{Ux}T_{Ijklm} \ddot{\eta}_j \xi_k \xi_l \xi_m \\
& + {}^{UU}T_{Ijklmn} \ddot{\eta}_j \xi_k \xi_l \xi_m \xi_n & + & {}^{UV}T_{Ijklmn} \ddot{\eta}_j \xi_k \eta_l \xi_m \xi_n \\
& + {}^{Vx}T_{Ijklm} \ddot{\eta}_j \eta_k \xi_l \xi_m & + & {}^{VU}T_{Ijklmn} \ddot{\eta}_j \eta_k \xi_l \xi_m \xi_n \\
& + {}^{VV}T_{Ijklmn} \ddot{\eta}_j \eta_k \eta_l \xi_m \xi_n & + & {}^{Vx}T_{Ijklm} \dot{\eta}_j \dot{\eta}_k \xi_l \xi_m \\
& + {}^{VU}T_{Ijklmn} \dot{\eta}_j \dot{\eta}_k \xi_l \xi_m \xi_n & + & {}^{VV}T_{Ijklmn} \dot{\eta}_j \dot{\eta}_k \eta_l \xi_m \xi_n \\
& + {}^{xV}T_{Ijklm} \dot{\eta}_j \dot{\eta}_k \xi_l \xi_m & + & {}^{UV}T_{Ijklmn} \dot{\eta}_j \xi_k \eta_l \xi_m \xi_n \\
& + {}^{VV}T_{Ijklmn} \dot{\eta}_j \eta_k \dot{\eta}_l \xi_m \xi_n,
\end{aligned}$$

where

$$\begin{aligned}
{}^2 T_{IJ} &= 4z_0^2 V_{iI} T_{ijkl} V_{jJ} x_{0,k} x_{0,l} \\
{}^3 T_{IJK} &= 4z_0^2 V_{iI} T_{ijkl} V_{jJ} x_{0,k} U_{lL} \\
{}^3 T_{IJK} &= 4z_0^2 V_{iI} T_{ijkl} V_{jJ} x_{0,k} V_{lL} \\
{}^3 T_{IJK} &= 4z_0^2 V_{iI} T_{ijkl} V_{jJ} U_{kK} x_{0,l} \\
{}^4 T_{IJKL} &= 4z_0^2 V_{iI} T_{ijkl} V_{jJ} U_{kK} U_{lL} \\
{}^4 T_{IJKL} &= 4z_0^2 V_{iI} T_{ijkl} V_{jJ} U_{kK} V_{lL} \\
{}^3 T_{IJK} &= 4z_0^2 V_{iI} T_{ijkl} V_{jJ} V_{kK} x_{0,l} \\
{}^4 T_{IJKL} &= 4z_0^2 V_{iI} T_{ijkl} V_{jJ} V_{kK} U_{lL} \\
{}^4 T_{IJKL} &= 4z_0^2 V_{iI} T_{ijkl} V_{jJ} V_{kK} V_{lL}, \\
{}^3 T_{IJK} &= 8z_0 U_K^z V_{iI} T_{ijkl} V_{jJ} x_{0,k} x_{0,l} \\
{}^4 T_{IJKL} &= 8z_0 U_L^z V_{iI} T_{ijkl} V_{jJ} x_{0,k} U_{lL} \\
{}^4 T_{IJKL} &= 8z_0 U_L^z V_{iI} T_{ijkl} V_{jJ} x_{0,k} V_{lL} \\
{}^4 T_{IJKL} &= 8z_0 U_L^z V_{iI} T_{ijkl} V_{jJ} U_{kK} x_{0,l} \\
{}^5 T_{IJKLM} &= 8z_0 U_M^z V_{iI} T_{ijkl} V_{jJ} U_{kK} U_{lL} \\
{}^5 T_{IJKLM} &= 8z_0 U_M^z V_{iI} T_{ijkl} V_{jJ} U_{kK} V_{lL} \\
{}^4 T_{IJKL} &= 8z_0 U_L^z V_{iI} T_{ijkl} V_{jJ} V_{kK} x_{0,l} \\
{}^5 T_{IJKLM} &= 8z_0 U_M^z V_{iI} T_{ijkl} V_{jJ} V_{kK} U_{lL} \\
{}^5 T_{IJKLM} &= 8z_0 U_M^z V_{iI} T_{ijkl} V_{jJ} V_{kK} V_{lL}, \\
{}^4 T_{IJKL} &= 4U_K^z U_L^z V_{iI} T_{ijkl} V_{jJ} x_{0,k} x_{0,l} \\
{}^5 T_{IJKLM} &= 4U_L^z U_M^z V_{iI} T_{ijkl} V_{jJ} x_{0,k} U_{lL} \\
{}^5 T_{IJKLM} &= 4U_L^z U_M^z V_{iI} T_{ijkl} V_{jJ} x_{0,k} V_{lL} \\
{}^5 T_{IJKLM} &= 4U_L^z U_M^z V_{iI} T_{ijkl} V_{jJ} U_{kK} x_{0,l} \\
{}^6 T_{IJKLMN} &= 4U_M^z U_N^z V_{iI} T_{ijkl} V_{jJ} U_{kK} U_{lL} \\
{}^6 T_{IJKLMN} &= 4U_M^z U_N^z V_{iI} T_{ijkl} V_{jJ} U_{kK} V_{lL} \\
{}^5 T_{IJKLM} &= 4U_L^z U_M^z V_{iI} T_{ijkl} V_{jJ} V_{kK} x_{0,l} \\
{}^6 T_{IJKLMN} &= 4U_M^z U_N^z V_{iI} T_{ijkl} V_{jJ} V_{kK} U_{lL} \\
{}^6 T_{IJKLMN} &= 4U_M^z U_N^z V_{iI} T_{ijkl} V_{jJ} V_{kK} V_{lL},
\end{aligned}$$

and

$$T_{IJKL} = -\frac{\pi}{4} \rho \omega A_{mJ} R_{mp} B_{pK} R_{Is} B_{sL}.$$

C Additional simulation results

This section provides robustness checks regarding the simulation results presented in Section 6.1, grouped in three analysis. Firstly, Section C.1 extends the comparison between the FOM and the (P)ROMs for an alternative muscle placement. Secondly, Section C.2 compares the ROB used in Section 6.1.2 to two other alternatives. Thirdly, the convergence of the solver and its solutions is analyzed in Section C.3.

C.1 Model comparisons: error profiles

When comparing the simulation results from the FOM to the ones of the ROM, Figure 8 reports relative errors between -10 and 15%. While the relative error grows for smaller tail oscillation, the absolute error remains small (Figure 16).

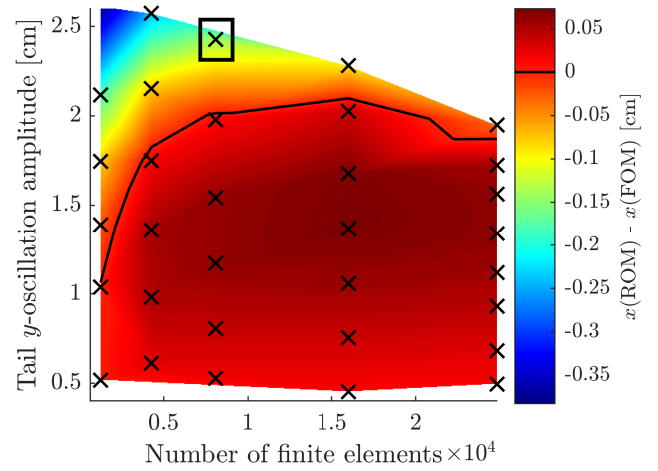


Figure 16. Absolute error in the swimming distance after $t = 2s$ between the FOM and the ROM for multiple discretizations and oscillation's amplitudes of the nominal shape (see Figure 6). The crosses indicate simulations results, and the heat map is obtained using a linear interpolation between these results. Simulations of the FOM performed in the white area in the top right corner (i.e., for large number of FEs and large oscillations) did not converge. The rectangle corresponds to the relative error measured in Figure 7.

To understand if these results are dependent on the muscle placement along the fish body, we consider the alternative arrangement shown in Figure 17. The relative errors between the FOM and ROM simulations have a similar magnitude than the results in Section 6.1.4, with errors between -15% and 5% for most combinations of oscillation and FE number (Figure 18). This increases the confidence in the reduced simulation results.

C.2 ROB selection analysis

As shown in Section 6.1.4, and in particular in Figure 7 and Figure 8, using a (P)ROM instead of the FOM yields small errors regarding the tail oscillation and the swimming distance. In the following, we investigate how the ROB selection presented in Section 6.1.2 impacts these errors. We consider two variations of the ROB: (1) a ROB with the first VM but no MDs, and (2) a ROB with the first 2 VMs and their corresponding MDs. We select 6 combinations of

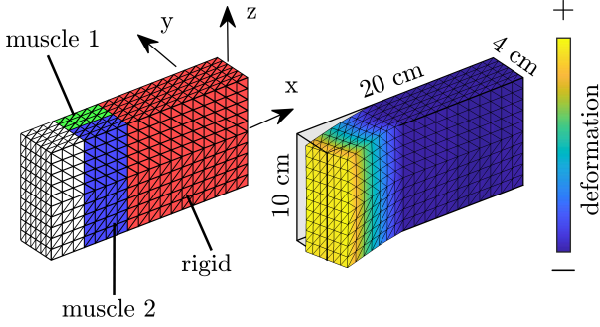


Figure 17. Alternative muscle placements (left) and corresponding vibration mode (right) used to obtain the error profile [Figure 18](#).

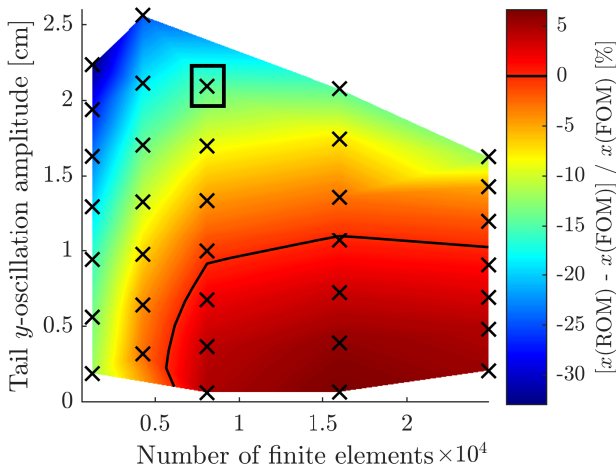


Figure 18. Relative error in the swimming distance after $t = 2s$ between the FOM and the ROM for multiple discretizations and oscillation's amplitudes of the nominal shape with alternative muscle placement (see [Figure 17](#)).

mesh discretizations and actuation stiffnesses, and compare the results obtained using the FOM and the ROM. These combinations consists of the case marked with a rectangle in [Figure 8](#), as well as the cases around it (marked with crosses).

The results are presented in [Table 5](#) and [Table 6](#), where the third column is the reference ROB used in [Section 6.1.2](#), and the fourth column the alternative selection. Compared to the ROB used in [Section 6](#), the ROB (1) without MDs shows poorer performance. The MDs allow to capture part of the nonlinearities of the FOM, which is not possible when using the first VM only. The ROB (2) with 2 VMS and their corresponding MDS is only marginally different than the ROB used in [Section 6](#). This can easily be explained by the fact that the second VM, shown in [Figure 19](#), is perpendicular to the deformation of the fish, and is in fact not activated when the fish is swimming.

While adding VMs are not improving the accuracy of the ROM in this particular case, the choice of the ROB ultimately depends on the robotic system being modeled. More complex systems, such as the robotic arms used by [Katzschmann et al. \(2019b\)](#) for example, would require a more expressive ROB with more VMs and MDs.

Table 5. Relative error comparison between the FOM and two ROMs based on different ROB: a ROB with one VM and its corresponding MDs (reference, [Section 6.1.2](#)), and a ROB with one VM but no MDs.

# FEs	Tail oscillation [cm]	Rel.% error w/ MDs	Rel.% error w/o MDs
4270	2.1533	-3.9528	-42.2850
4270	1.7495	1.2814	-46.0000
8086	2.4272	-5.9964	-45.2700
8086	1.9787	0.7696	-50.0070
16009	2.0252	2.1396	-50.0420
16009	1.6775	6.0262	-39.6960

Table 6. Relative error comparison between the FOM and two ROMs based on different ROB: a ROB with one VM and its corresponding MDs (reference, [Section 6.1.2](#)), and a ROB with two VMs and MDs.

# FEs	Tail oscillation [cm]	Rel.% error 1 VM	Rel.% error 2VMs
4270	2.1533	-3.9528	-3.5768
4270	1.7495	1.2814	1.5406
8086	2.4272	-5.9964	-5.4423
8086	1.9787	0.7696	1.1668
16009	2.0252	2.1396	2.5219
16009	1.6775	6.0262	6.3103

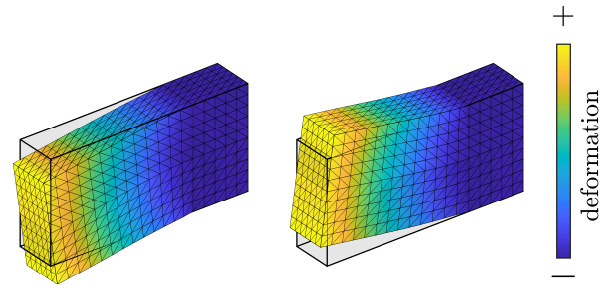


Figure 19. Second vibration mode, with a deformation perpendicular to the oscillation of the tail.

C.3 Simulation convergence

This section presents an analysis of the time stepping scheme followed in the simulations, assessing the convergence of the integration scheme and the validity of the used time step of 0.02s.

Considering the nominal shape discuss in [Section 6.1](#), we solve the EoMs and obtain the sensitivities for the PROM with 5 parameters for three different integration time steps: $h = 0.02s$, $h = 0.01s$, $h = 0.005s$. Firstly, [Figure 20](#) shows that the refinement of the time step does not change the physical behavior of the system.

Secondly, we compute the following errors evaluated at common time instants

$$e_{0.02 \rightarrow 0.01}(t) = u_{0.02}(t) - u_{0.01}(t),$$

$$e_{0.01 \rightarrow 0.005}(t) = u_{0.01}(t) - u_{0.005}(t),$$

where u is the head x -position for the different integration time steps ($h = 0.02s$, $h = 0.01s$, $h = 0.005s$). Taking the

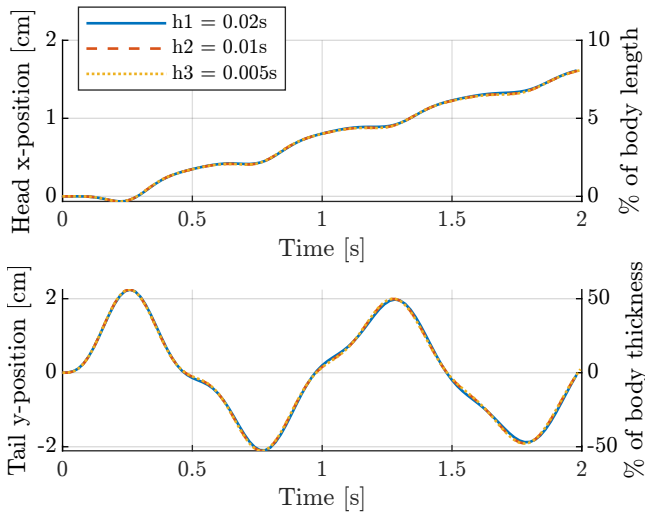


Figure 20. Trajectories of the nominal shape for different integration time steps, obtained using the PROM with 5 parameters.

L2 norm over the vectors of errors gives the refinement ratio

$$\rho = \frac{E_{0.02 \rightarrow 0.01}}{E_{0.01 \rightarrow 0.005}} = \frac{\|e_{0.02 \rightarrow 0.01}\|_2}{\|e_{0.01 \rightarrow 0.005}\|_2} = 3.6,$$

which is consistent with second-order convergence, as expected using the Newmark- β integration scheme. The solver therefore operates in asymptotic regime.

Finally, we follow a similar procedure to show the convergence of the parameter sensitivities (19). Sensitivities being matrices, we compute the Frobenius norm at each time step:

$$e_{0.02 \rightarrow 0.01}(t) = \|S_{0.02}(t) - S_{0.01}(t)\|_F,$$

$$e_{0.01 \rightarrow 0.005}(t) = \|S_{0.01}(t) - S_{0.005}(t)\|_F.$$

The resulting refinement ratio is

$$\rho = \frac{E_{0.02 \rightarrow 0.01}}{E_{0.01 \rightarrow 0.005}} = \frac{\|e_{0.02 \rightarrow 0.01}\|_2}{\|e_{0.01 \rightarrow 0.005}\|_2} = 2.7,$$

which also demonstrates monotonic convergence of the sensitivities under time step refinement. Together, these results confirm correct solver behavior and justify the time step of $h = 0.02$ s.

D Additional optimization results

This section presents additional optimization results that zoom into the parameters' initialization (Section D.1), the quality of the PROM approximations and the related gradients (Section D.2), and the extension of the shape optimization to a larger design space (Section D.3)

D.1 Optimization initialization

To assess how the shape parameters' initialization affects the optimization results, we run SO1-SO3 using two random sets of initial parameters. The obtained optimal shapes are similar to the results obtained in Section 6.2, as reported in Table 7 (SO1), Table 8 (SO2), and Table 9 (SO3). The final costs are also identical, but the optimization trajectories might differ based on the parameter initialization (Figures 21 to 23).

Table 7. Shape optimization results obtained with different initializations of the parameters for SO1. The columns denoted 'main' contain the results presented in Section 6.2 and the columns denoted '1' and '2' contain results for two other parameters' initializations.

	Initialization			Optimized parameters		
	main	1	2	main	1	2
ξ_1	0	-0.01	-0.16	-0.5	-0.5	-0.5
ξ_2	0	-0.06	-0.37	0.29	0.28	0.27
ξ_3	0	-0.13	-0.09	0.15	0.15	0.15

Table 8. Shape optimization results obtained with different initializations of the parameters for SO2. The columns denoted 'main' contain the results presented in Section 6.2 and the columns denoted '1' and '2' contain results for two other parameters' initializations.

	Initialization			Optimized parameters		
	main	1	2	main	1	2
ξ_1	0	-0.01	-0.16	-0.49	-0.50	-0.50
ξ_2	0	-0.06	-0.37	0.32	0.31	-0.44
ξ_4	0	-0.13	-0.09	0.39	0.40	0.40
ξ_5	0	-0.06	-0.37	0.49	0.48	0.49
ξ_6	0	-0.13	-0.09	0.49	0.49	0.49

Table 9. Shape optimization results obtained with different initializations of the parameters for SO3. The columns denoted 'main' contain the results presented in Section 6.2 and the columns denoted '1' and '2' contain results for two other parameters' initializations.

	Initialization			Optimized parameters		
	main	1	2	main	1	2
ξ_1	0	-0.01	-0.16	-0.50	-0.50	-0.50
ξ_2	0	-0.06	-0.37	0.32	0.37	0.42
ξ_4	0	-0.13	-0.09	0.30	0.29	0.30
ξ_5	0	-0.06	-0.37	0.39	0.39	0.38
ξ_6	0	-0.13	-0.09	0.38	0.37	0.39
ξ_7	0	-0.06	-0.37	0.24	0.25	0.25
ξ_8	0	-0.13	-0.09	0.245	0.25	0.25
ξ_9	0	-0.06	-0.37	0.17	0.18	0.18

D.2 Quality of PROM approximations

The optimization pipeline Figure 5 uses the PROM to compute gradients and approximate the solution of the EoMs for shape morphologies described by parameters that are close to the one of the nominal shape. If the current shape-varied mesh is too different from the nominal shape, the approximation of the system's dynamics using the sensitivities (21) might not be accurate.

In the optimization pipeline, the approximation of the system's motion is important to obtain the gradient with which we update the parameters. We are therefore not interested in obtaining a good approximation of the EoMs

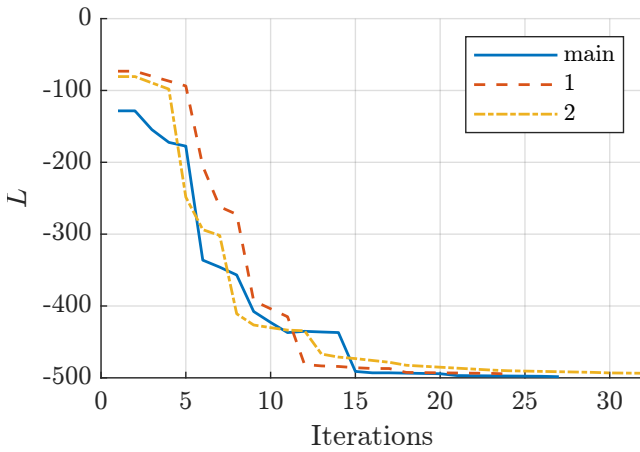


Figure 21. Cost function for SO1 with different random initializations of the search parameters (see Table 7).

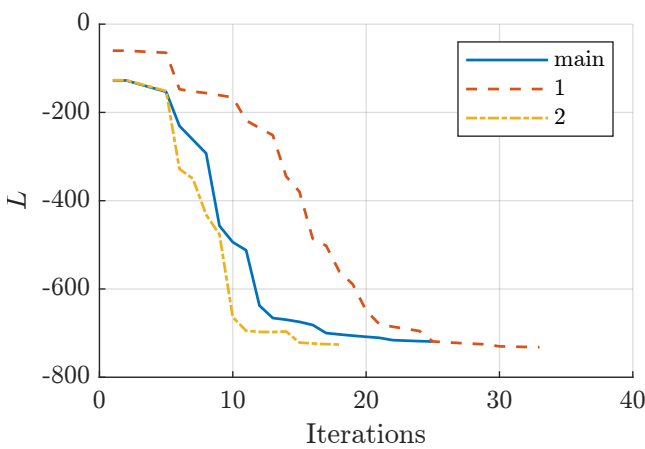


Figure 22. Cost function for SO2 with different random initializations of the search parameters (see Table 8).

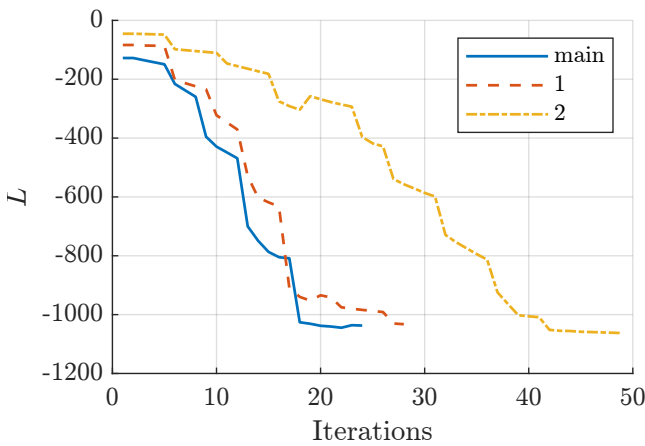


Figure 23. Cost function for SO3 with different random initializations of the search parameters (see Table 9).

solutions *per se*, but rather by the gradient computed based on this approximation. If this quantity departs too drastically from the value that a local PROM build for the current mesh would provide, we would like to rebuild a PROM.

The current implementation let the user define two thresholds that control when a PROM is rebuilt. First, if any of the shape parameter deviates more than `rebuildThreshold` from the parameter used for the

last EoMs solve, a new PROM is constructed and the EoMs are re-solved. Second, a rebuild is triggered once a maximum number of iterations, specified by `nRebuild`, is reached. These parameters define a trade-off between computational effort and model fidelity: larger thresholds reduce the number of PROM reconstructions and EoMs solves, improving efficiency, whereas smaller thresholds maintain closer agreement between the reduced model and the current shape parameters, yielding more accurate state predictions and gradients. The choice of these parameters ultimately depends on the complexity of the optimization landscape.

The shape optimization experiments presented in Section 6.2 use `rebuildThreshold=0.15` and `nRebuild=5` or `nRebuild=6`. To assess the quality of the approximations and gradients obtained by the PROM under these specifications, we consider the case SO2, which cost function evolution is shown in Figure 24. Uppercase letters denote iteration at which a new PROM has been built. Lowercase letters represent selected midstep iterations at which approximations have been used. For each segment ‘iJ’, we compare two approximations obtained using the sensitivities (21) to ground-truth results obtained with local PROMs.

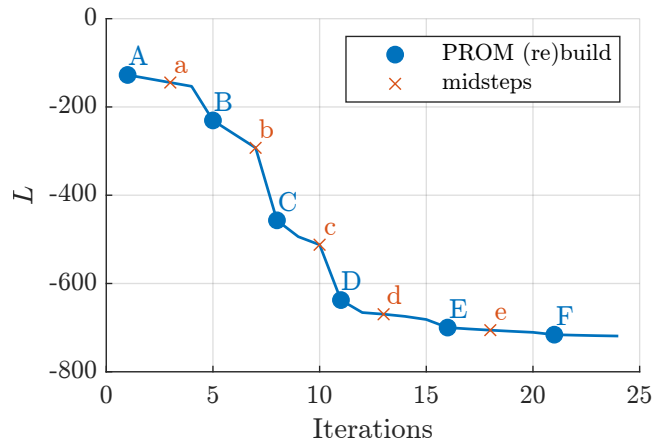


Figure 24. Cost function of SO1. Iterations at which a PROM is built are marked with circle and capital letters. Crosses indicates selected iterations at which approximation using PROM’s sensitivities are used.

The PROM approximations are characterized by three features according to our results. First, their quality is poorer for segments ‘iJ’ at which a large cost decrease occurs (i.e., AaB, BbC, and CcD), and better close to convergence (DdE, EeF). Figure 25 illustrates this pattern. Second, the error from the approximation is smaller at midsteps, and larger at rebuild step, when a new PROM is in fact rebuilt (Figure 25, top panels, and Table 10). Third, the gradient obtained using the approximation is consistent in its direction with the ground truth gradient obtained by a local PROM, indicating that we can rely on the descent direction (Table 10).

D.3 Alternative shape variations

We present three additional case-studies focusing on shape optimization (SO7, SO8, and SO9). These cases use some of the shape variations depicted in Figure 10 as well as additional shape variations proposed in Figure 26. The exact

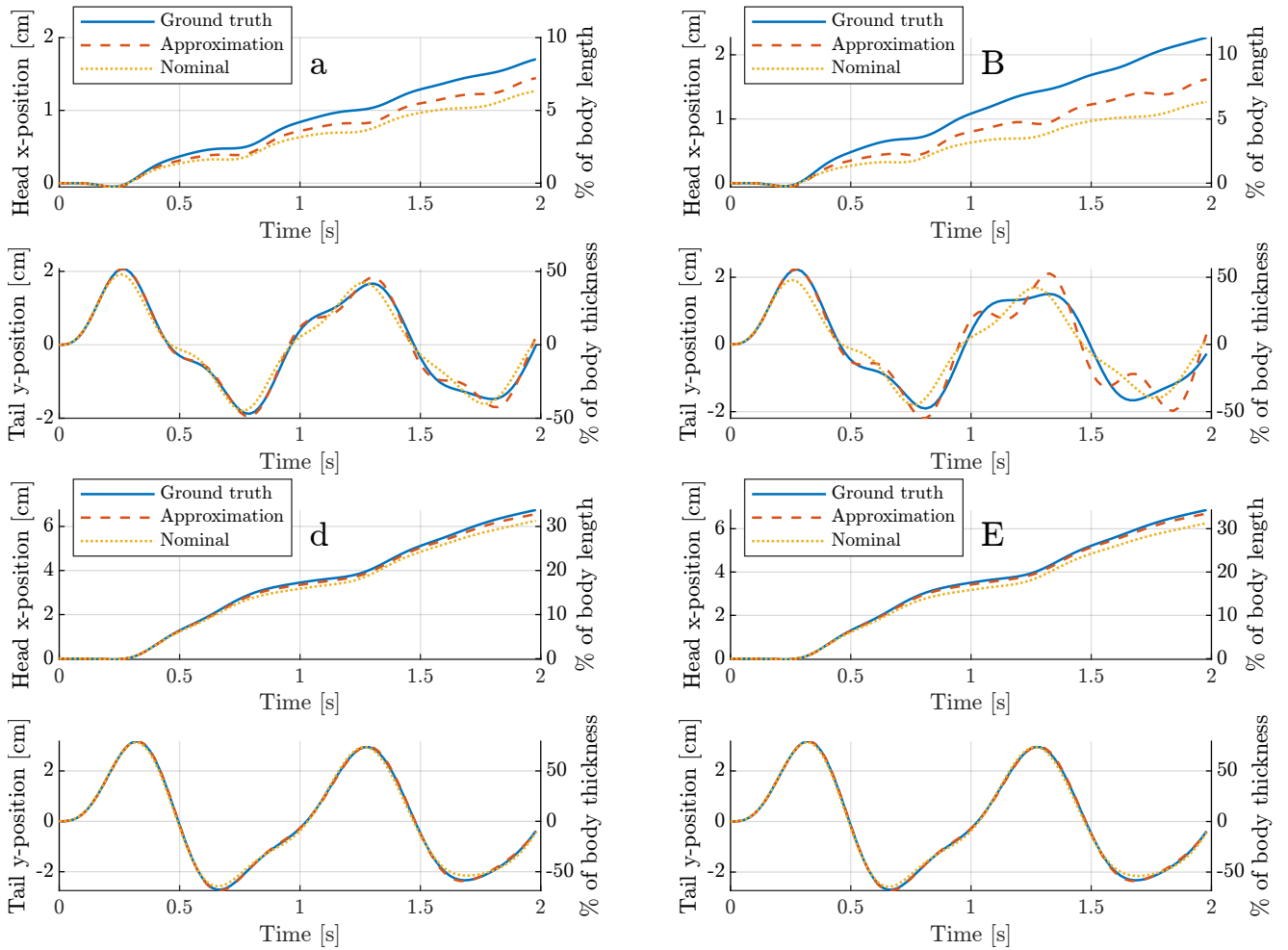


Figure 25. Comparison between ground truth motion provided by a local PROM and its approximation using sensitivities from a nominal PROM for selected iterations of SO2 (see Figure 24).

selection and constraints for each of the three cases is summarized in Table 11, resulting in cases with 5 or 6 optimization parameters.

First, we compare the results of SO7 and SO8, which both have 5 shape variations that represent lateral features of the fish. While SO7 comprises a lateral notch (ξ_{11}) and a fin (ξ_{10}), SO8 comprises the feature of a thinner lateral tail (ξ_4) and rounded corners (ξ_6). While SO8 fully uses the search space and hits the constraints (Figure 28, parameters of interest highlighted in gray), SO7 does not heavily use the fin and the notch features (Figure 27). The swimming distance is also considerably larger for SO8 compared to SO7 (9.1cm compared to 6.3cm).

This example shows that not only the number of shape variations matters for the optimal swimming performance, but also their ability to express meaningful features. While the optimization pipeline can accommodate any type of shape variations, they should be chosen according with some knowledge of the test case to be expressive.

The last example provided by SO9 focuses on the feature selection of a tail under active design constraint. Three possible tail features can be combined ($\xi_1, \xi_{12}, \xi_{13}$) but the height of the tail tip cannot exceed a certain threshold, leading to the joint constraint $-0.8 \leq \xi_1 + \xi_{12} + \xi_{13} \leq 0.8$. The optimizer therefore has to weight competing designs for a limited amount of physical space. The resulting

morphology is shown in Figure 29 and reached 7.3 cm. As shown in the gray cells of Figure 29, the optimizer uses mainly the shape variation 1 and 13, but leaves the feature 12 aside. Such an example shows that the pipeline can be practically useful to decide between competing morphological features.

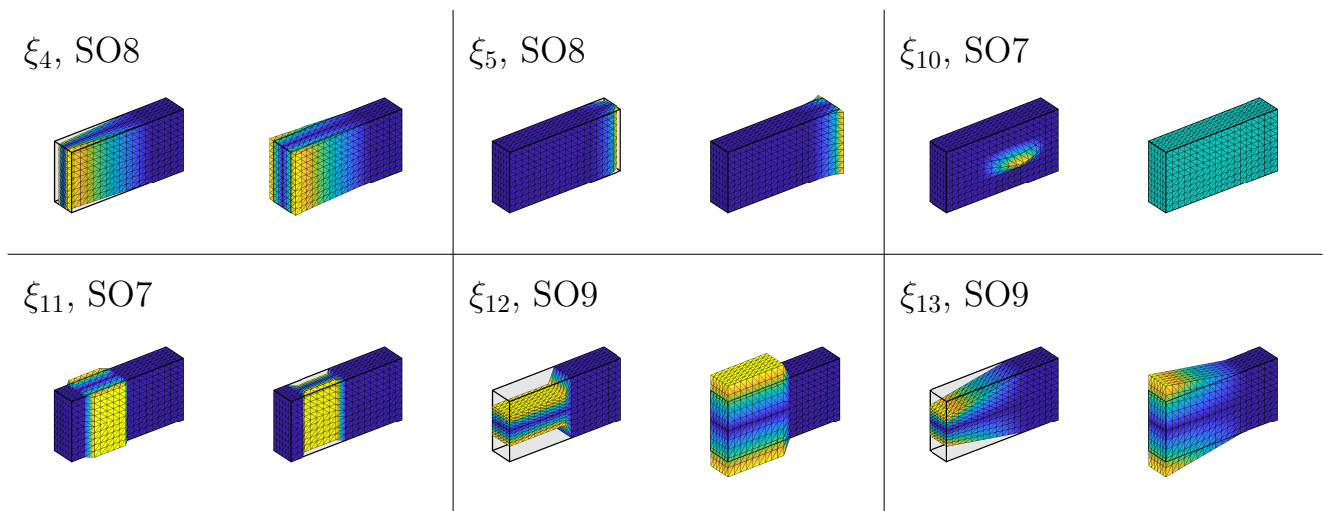


Figure 26. Additional shape variations used in the numerical experiments described in Section D.3.

Table 10. Comparison between the gradients obtained with PROM approximations ($\bar{\nabla}L$) and ground truth local PROMs (∇L) for selected iterations of SO2 (see Figure 24).

It.	∇L	$\bar{\nabla}L$	Rel. error [%]	Δ angle [°]
a	137	112	-18	7.4
	-16	-11	30	
	-121	-76	37	
	-16	-11	32	
	-81	-54	34	
B	168	112	-33	13.2
	-23	-11	51	
	-186	-76	59	
	-24	-11	54	
	-118	-54	55	
d	324	295	-9	4.4
	-53	-66	-25	
	-747	-692	7	
	-88	-92	-5	
	-198	-243	-22	
E	323	295	-9	5.28
	-30	-66	-118	
	-774	-692	11	
	-68	-92	-37	
	-209	-243	-16	

Table 11. Lower and upper bound on the search parameters for shape optimization experiments SO7-SO9.

Case	SO7	SO8	SO9
ξ_1	-0.5, 0.5	-0.5, 0.5	-0.5, 0.5
ξ_2	-0.5, 0.5	-0.5, 0.5	-0.5, 0.5
ξ_3	-0.15, 0.15	-0.15, 0.15	not used
ξ_4	not used	-0.4, 0.4	-0.4, 0.4
ξ_5	not used	-0.4, 0.4	not used
ξ_6	not used	not used	-0.4, 0.4
ξ_{10}	-0.02, 0.3	not used	not used
ξ_{11}	-0.3, 0.3	not used	not used
ξ_{12}	not used	not used	-0.5, 0.5
ξ_{13}	not used	not used	-0.5, 0.5

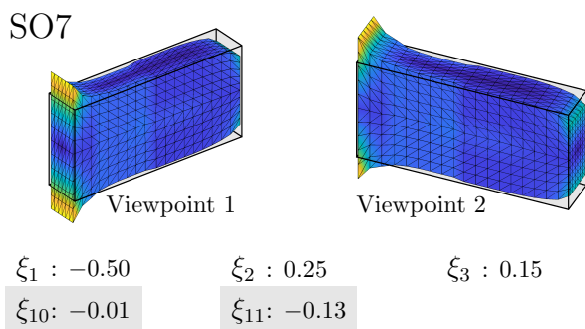


Figure 27. Optimal shape obtained for SO7.

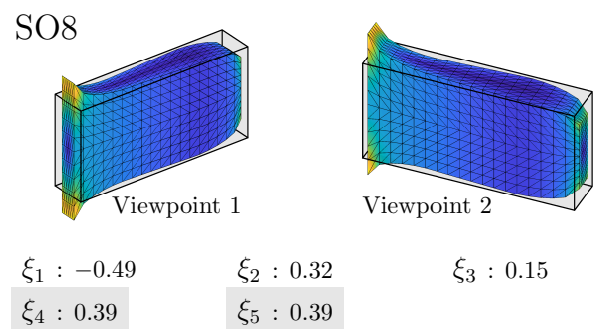


Figure 28. Optimal shape obtained for SO8.

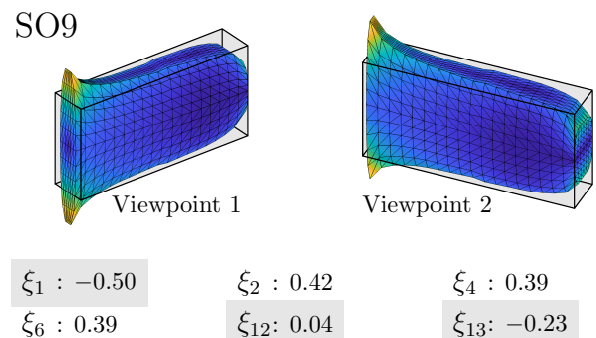


Figure 29. Optimal shape obtained for SO9.